Influence of temporally varying weatherability on CO₂–climate coupling and ecosystem change in the late Paleozoic.

Jon D. Richey[1*], Isabel P. Montañez[1*], Yves Goddéris[2], Cindy V. Looy[3], Neil P. Griffis[1,4], William A. DiMichele[5]

[1]Department of Earth and Planetary Sciences, University of California, Davis, Davis, CA 95616, USA.
[2]Géosciences Environnement Toulouse, CNRS – Université Paul Sabatier, Toulouse, France.
[3]Department of Integrative Biology and Museum of Paleontology, University of California, Berkeley, Berkeley, CA 94720, USA.
[4]Berkeley Geochronology Center, Berkeley, CA 94720, USA.
[5]Department of Paleobiology, Smithsonian Museum of Natural History, Washington, DC 20560, USA.

Correspondence to: Jon D. Richey (jdrichey@ucdavis.edu); Isabel P. Montañez (ipmontanez@ucdavis.edu)

Abstract Earth's penultimate icehouse, the Late Paleozoic Ice Age (LPIA), was a time of dynamic glaciation and repeated ecosystem perturbation, under conditions of substantial variability in atmospheric pCO_2 and O_2. Improved constraints on the evolution of atmospheric pCO_2 and $O_2:CO_2$ during the LPIA and its subsequent demise to permanent greenhouse conditions is crucial for better understanding the nature of linkages between atmospheric composition, climate, and ecosystem perturbation during this time. We present a new and age-recalibrated pCO_2 reconstruction for a 40-Myr interval (~313 to 273 Ma) of the late Paleozoic that (1) confirms a previously hypothesized strong CO₂-glaciation linkage, (2) documents synchroneity between major pCO_2 and $O_2:CO_2$ changes and compositional turnovers in terrestrial and marine ecosystems, (3) lends support for a modeled progressive decrease in the CO_2 threshold for initiation of continental ice sheets during the LPIA, and (4) indicates a likely role of CO_2 and $O_2:CO_2$ thresholds in floral ecologic turnovers. Modeling of the relative role of CO_2 sinks and sources active during the LPIA and its demise on steady-state pCO_2 using an intermediate complexity climate-C cycle model (GEOCLIM) and comparison to the new multi-proxy CO_2 record provides new insight into the relative influences of the uplift of the Central Pangean Mountains, intensifying aridification, and increasing mafic rock to-granite rock ratio of outcropping rocks on the global efficiency of CO_2 consumption and secular change in steady-state pCO_2 through the late Paleozoic.

1 Introduction

Earth's penultimate and longest-lived icehouse (340 to 290 Ma) occurred under the lowest atmospheric CO_2 concentrations

of the last half-billion years (Foster et al., 2017) and, potentially, the highest atmospheric pO_2 of the Phanerozoic (Glasspool

et al., 2015; Krause et al., 2018; Lenton et al., 2018). Anomalous atmospheric composition, along with 3% lower solar

luminosity (Crowley and Baum, 1992), may have primed the planet for a near-miss global glaciation (Feulner, 2017).

Notably, Earth's earliest tropical forests assembled and expanded during this icehouse (the Late Paleozoic Ice Age; LPIA),

leading to the emergence of large-scale wildfire. Paleotropical terrestrial ecosystems underwent repeated turnovers in

composition and architecture, culminating in the collapse of wetland (coal) forests throughout tropical Pangea at the close of

the Carboniferous (Cleal and Thomas, 2005; DiMichele, 2014), possibly promoting the diversification and ultimate

dominance of amniotes (Pardo et al., 2019). In the marine realm, global rates of macroevolution (origination, extinction)

decreased, in particular among tropical marine invertebrates, and genera with narrow latitudinal ranges went extinct at the

onset of the LPIA (Stanley, 2016; Balseiro and Powell, 2019). Low marine macroevolutionary rates continued through to the

demise of the LPIA in the early Permian (Stanley and Powell, 2003; McGhee, 2018).

Reconstructions of late Paleozoic atmospheric pCO_2 document a broad synchroneity between shifts in CO_2, glaciation

history, glacioeustasy, and restructuring of paleotropical biomes, underpinning the hypothesized greenhouse-gas forcing of

sub-million-year glacial-interglacial cycles (Montañez et al., 2016) and the terminal demise of the LPIA (Montañez et al.,

2007). For late Paleozoic pCO_2 (and pO_2) reconstructions, however, broad intervals of low temporal resolution and

significant uncertainties limit the degree to which mechanistic linkages between atmospheric composition, climate, and

ecosystem change can be further evaluated. Moreover, the potential impact of large magnitude fluctuations in atmospheric

O_2:CO_2, which characterized the late Paleozoic, on the biosphere has been minimally addressed. On longer timescales ($\geq 10^6$

yr), the relative role of potential CO_2 sinks and sources on secular changes in late Paleozoic atmospheric CO_2 and, in turn, as

drivers of glaciation and its demise, remain debated (McKenzie et al., 2016; Goddéris et al., 2017; Macdonald et al., 2019).

Here, we present a multi-proxy atmospheric pCO_2 reconstruction for a 40-Myr interval (313 to 273 Ma) of the late

Paleozoic, developed using new leaf fossil-based estimates integrated with recently published and age-recalibrated

Pennsylvanian pCO_2 estimates of 10^5-yr resolution (Montañez et al., 2016), and re-evaluated fossil soil (paleosol) based CO_2

56 estimates for the early Permian (Montañez et al., 2007). Our new multi-proxy record offers higher temporal resolution than

57 existing archives while minimizing and integrating both temporal and CO_2 uncertainties. This $p$$CO_2$ reconstruction, together

58 with new O_2:CO_2 estimates of similar temporal resolution, permits refined interrogation of the potential links between

59 fluctuations in atmospheric composition, climate shifts, and ecosystem events through Earth's penultimate icehouse.

60 Moreover, comparison of the new 40-Myr CO_2 record with modeled steady-state $p$$CO_2$ and seawater ^{87}Sr/^{86}Sr over the same

61 interval provides new insight into the relative importance and evolution of CO_2 sinks and sources during late Paleozoic

62 glaciation and its turnover to a permanent greenhouse state.

63

64 **2 Materials and Methods**

65 A brief account of the methods is presented here; more details are presented in the Supplementary Materials and Methods.

66 Primary data generated or used in this study are deposited in the Dryad Digital Repository (Richey et al., 2020) and can be

67 accessed at https://doi.org/10.25338/B8S90Q.

68

69 **2.1 Sample Collection and Analysis**

70 To build the $p$$CO_2$ record, 15 plant cuticle fossil species/morphotypes were used, collected from eight localities in Illinois,

71 Indiana, Kansas, and Texas, USA, including four well-studied Pennsylvanian interglacial floras (Sub-Minshall [313 Ma;

72 Šimůnek, 2018], Kinney Brick [305.7 Ma; DiMichele et al., 2013], Lake Sarah Limestone [303.7 Ma; Šimůnek, 2018], and

73 Hamilton Quarry [302.7 Ma; Hernandez-Castillo et al., 2009a, b, c]; Figs. 1a, S2–4, Richey et al., 2020,

74 https://doi.org/10.25338/B8S90Q). The Pennsylvanian estimates were integrated into a previously published $p$$CO_2$

75 reconstruction (313 to 296 Ma; Montañez et al., 2016) of 10^5-yr resolution built using pedogenic carbonates and wet-adapted

76 seed fern fossils (Figs. 2b, S1b). The Permian estimates were integrated with previously published latest Carboniferous and

77 early Permian pedogenic carbonate-based CO_2 estimates (Montañez et al., 2007), derived from paleosols from successions

78 throughout Arizona, New Mexico, Oklahoma, Texas, and Utah, USA (Fig. 1a, Richey et al., 2020,

79 https://doi.org/10.25338/B8S90Q). The pedogenic carbonates and leaf cuticle fossils span a broad region of Pennsylvanian

80 and early Permian tropical Euramerica (Figs. 1b). Ages of samples used in Montañez et al., (2007) and (2016) were

81 recalibrated and assigned uncertainties using the latest geologic timescale (Ogg et al., 2016) and biostratigraphic and

82 geochronologic controls (see Supplementary Materials and Methods; Richey et al., 2020, https://doi.org/10.25338/B8S90Q).

83   Cuticle and organic matter occluded within pedogenic carbonates (OOM) were rinsed or dissolved, respectively, in 3M

84 HCl to remove carbonates and analyzed at the Stable Isotope Facility, University of California, Davis, using a PDZ Europa

85 ANCA-GSL elemental analyzer interfaced to a PDZ Europa 20-20 IRMS. External precision, based on repeated analysis of

86 standards and replicates, is $<\pm0.2‰$. For Hamilton Quarry (HQ), all material was previously mounted on slides for

87 taxonomic analysis (Hernandez-Castillo et al., 2009a; Hernandez-Castillo et al., 2009b, c). Because of this, biomarker $\delta^{13}C$

88 values of bulk stratigraphic sediment samples were used (Richey et al., unpublished data; see Supplementary Materials and

89 Methods). HQ n-$C_{27–31}$ n-alkane $\delta^{13}C$ was analyzed using a Thermo Scientific GC-Isolink connected to a Thermo Scientific

90 MAT 253. Standard deviation of n-alkane $\delta^{13}C$ was $\pm0.3‰$. For biomarker $\delta^{13}C$, a +4‰ correction was used to account for

91 fractionation during biosynthesis (Diefendorf et al., 2015) and the standard deviation of all values was used as the

92 uncertainty (1.6‰, five times the analytical precision).

93

94 **2.2 Models**

95 The MATLAB model Paleosol Barometer Uncertainty Quantification (PBUQ; Breecker, 2013), which fully propagates

96 uncertainty in all input parameters, was used to derive pedogenic carbonate-based CO_2 estimates (Figs. 2a, S1a). For each

97 locality, paleosols of inferred different soil orders were modeled separately. We applied improved soil-specific values for

98 soil-respired CO_2 concentrations ($S_{(z)}$; Montañez, 2013) and the $\delta^{13}C$ of organic matter occluded within carbonate nodules

99 ($\delta^{13}C_{OOM}$; Fig. S5) as a proxy of soil-respired CO_2 $\delta^{13}C$. For samples where OOM was not recovered, estimates were revised

100 using PBUQ and the plant fossil organic matter $\delta^{13}C$ used in Montañez et al., (2007) ($\delta^{13}C_{POM}$; Fig. S5). Because of the

101 limited amount of carbonate nodules remaining after study by Montañez et al., (2007), $\delta^{13}C_{OOM}$ was substituted for $\delta^{13}C_{POM}$

102 for localities that occur in the same geologic formation and a large error ($\pm$ 2‰) was used to account for the uncertainty in

103 this approach. PBUQ model runs conducted in this study resulted in a small subpopulation of biologically untenable CO_2

104 estimates (i.e., $\leq$170 ppm; Gerhart and Ward, 2010). To limit estimates below that threshold, two changes to the PBUQ

105 Matlab code were made (see Supplementary Materials and Methods for details). All other input parameters remained

4

106   unchanged from Montañez et al., (2007).

107   For cuticle fossil-based (Figs. S2–4) CO_2 estimates (Fig. 2a, S1a), we utilized a mechanistic (non-taxon-specific) gas-

108   exchange model (Franks et al., 2014). For some fossil cuticles, pore length (PL) was measured directly; for others, PL was

109   inferred from guard cell length (GCL; Table S2). Guard cell width was estimated via GCL using the prescribed

110   gymnosperms and ferns scaler (0.6; Franks et al., 2014; Table S2).

111   For both stomatal and pedogenic-carbonate-based CO_2 modeling, we calculated $\delta^{13}C$ of atmospheric CO_2 using the

112   carbonate $\delta^{13}C$ record generated from an open-water carbonate slope succession (Naqing succession, South China; Buggisch

113   et al., 2011), contemporaneous estimates of mean annual temperature (Tabor and Montañez 2005; Tabor et al., 2013), and

114   temperature-sensitive fractionation between low-Mg calcite and atmospheric CO_2 (Romanek et al., 1992; Eq. S2; Table S2).

115   We used the spatially resolved, intermediate complexity GEOCLIM model (Goddéris et al., 2014) to quantitatively

116   evaluate how steady-state atmospheric CO_2 may have responded to changes in weatherability and relative influence of

117   different CO_2 sources and sinks. The spatial distributions of the mean annual runoff and surface temperature were calculated

118   offline for five time increments (Goddéris et al., 2017) covering the period of interest and for various atmospheric CO_2 levels

119   using the 3D ocean-atmosphere climate model FOAM and the approach as described in Donnadieu et al., (2006). GEOCLIM

120   uses generated lookup tables to calculate steady-state atmospheric CO_2 for a given continental configuration and to account

121   for paleogeography and relief. Although GEOCLIM model does not include an explicit surface distribution of lithology,

122   weathering rate of mafic rocks and continental granites are calculated using different methods and the impact of physical

123   erosion on granite weathering is accounted for (Goddéris et al., 2017). For mafic surfaces, a simple parametric law is used,

124   linking the surface of the considered grid cell, the local runoff, and mean annual temperature to the local mafic weathering

125   rate. The calibration of the GEOCLIM model was performed at the continental-scale by tuning the parameters of the model

126   so that 30% of the alkalinity generated by the weathering of silicates originates from the weathering of mafic rocks

127   (GEOCLIM_REG; Dessert et al., 2001; Goddéris et al., 2014).

128

129   **2.3 O_2:CO_2**

130   O_2:CO_2 ratios (Fig. 3a) were calculated using the 10,000 CO_2 estimates produced by our modeling and combined with O_2

131   estimates obtained using geochemical mass balance and biogeochemical models (Krause et al., 2018; Lenton et al., 2018).

132   Unreasonably high $O_2:CO_2$ (generally those that correspond to CO_2 ~<200 ppm) were removed from the resulting 10,000

133     $O_2:CO_2$ data set.

134

135   **2.4 Statistical Analyses**

136   We utilize a bootstrap approach that assesses uncertainties of both CO_2 (or $O_2:CO_2$) and age. Each age uncertainty was

137   truncated to ensure no overlap in locality ages, constrained by their relative stratigraphic position to one another (Richey et

138   al., 2020; https://doi.org/10.25338/B8S90Q). The 10,000 modeled CO_2 estimates were trimmed by 28% to remove

139   anomalously high/low values. The means of the resulting 7,200 CO_2 estimates were compared to the trimmed means of the

140   10,000 CO_2 estimates to ensure that trimming did not alter the central tendency of the data. Locality ages were resampled

141   and perturbed, assuming that the individual ages and truncated age uncertainties represent the mean and standard deviation

142   of the ages. Similarly, the trimmed $CO_2/O_2:CO_2$ datasets were resampled and the resampled ages and estimates were used to

143   build 1000 resampled datasets. Each resampled dataset was subjected to LOESS analysis (0.25 smoothing) and the median

144   and 95% and 75% confidence intervals were calculated (Figs. 2, 3a–b, S1). The Pennsylvanian and Permian portions of the

145   record were analyzed separately due to differing data density, with significant overlap across the Pennsylvanian-Permian

146   boundary interval (Figs. 2b, 3b, S1b).

147   To test the validity of short-term fluctuations in the LOESS CO_2 trend, we undertook further analysis of the raw Monte

148   Carlo data produced by PBUQ and the mechanistic stomatal model in several short-term increments. Eleven short-term highs

149   or lows (A–K on Fig. 4A) were designated and used to form bins of ±0.5 to ±1 Myr. Within an individual bin, each shown

150   'bootstrapped' CO_2 data point is the trimmed mean of 10,000 Monte Carlo model runs. The Monte Carlo model runs for

151   each data point were sorted from lowest to highest CO_2 value and the lowest CO_2 values for each data point within the bin

152   were averaged. This averaging was repeated sequentially for each of the 10,000 values creating 10,000 means for each bin

153   (n=11). To evaluate whether a visually perceived rise or fall (e.g., A to B decrease or B and C increase) is statistically valid,

154   the 10,000 means of two adjacent bins were compared sequentially with one another (i.e., the mean of the lowest values of

155   one bin was compared to the mean of the lowest values of the adjacent bin) in order to calculate a percent change (((V_2 –

156 $V_1)/V_1$) * 100) for each of the 10,000 model runs, resulting in 10,000 percent changes for each set of adjacent bins. The

157 percent of the 10,000 comparisons that confirm an increase or decrease between bins is reported (Fig. 4B–J) as a measure of

158 the statistical significance of the short-term fluctuations in CO_2 concentration visually observed on the LOESS trend.

159

160 **3 Results**

161 Revised early Permian mineral-based CO_2 estimates define a substantially narrower range (45–1150 ppm; Fig. 2a) than

162 previous estimates (175–3500 ppm) made using the same pedogenic carbonate sample set (Montañez et al., 2007) while

163 maintaining the original trends and including fewer photosynthetically untenable concentrations ($\leq$170 ppm; Gerhart and

164 Ward, (2010)). New early Permian cuticle-based estimates show a high level of congruence by locality and broad plant

165 functional type, falling within the revised pedogenic-based CO_2 range (Figs. 2a, S1a). Similarly, stomatal-based estimates for

166 the four Pennsylvanian interglacial floras are within the estimated pCO_2 range defined by the pedogenic carbonates (Fig. 2a,

167 S1a) and late-glacial wetland plant fossils (Montañez et al., 2016). Notably, the newly integrated record confirms elevated

168 atmospheric CO_2 concentrations (482 to 713 ppm [-28/+72 ppm]) during Pennsylvanian interglacials in comparison to pCO_2

169 during glacial periods (161 to 299 ppm [-96/+269 ppm]), with interglacial durations on the order of 1000s to 10s of 1000s of

170 years given the inferred eccentricity scale duration of the glacial-interglacial cycles (Horton et al. 2012; Montañez et al.

171 2016; Fielding et al. 2020).

172 Overall, the new pCO_2 record documents declining CO_2 through the final 13-Myr of the Pennsylvanian into the earliest

173 Permian, including a 2.5-Myr interval (307 to 304.5 Ma) of minimum CO_2 values (less than 400 to as low as 200 ppm) in the

174 Kasimovian (Fig. 2b, S1b). Declining pCO_2 in the late Carboniferous coincides with rising atmospheric pO_2 (Glasspool et

175 al., 2015; Krause et al., 2018; Lenton et al., 2018); thus, O_2:CO_2 ratios in the interval of minimum Pennsylvanian CO_2 are

176 nearly two times those of present-day (~515; gray line in Fig. 3a). A 10-Myr CO_2 nadir (~180 to <400 ppm) characterizes the

177 first two stages (Asselian and Sakmarian; 298.9 to 290.1 Ma) of the early Permian, overlaps with the peak occurrence of

178 glacial deposits in the LPIA (gray boxes in Fig. 2b; Soreghan et al., 2019), and defines a second interval of anomalously high

179 O_2:CO_2 ratios (up to 970 ppm; Fig. 3a). A subsequent long-term rise (~17 Myr) in pCO_2 to peak values up to ~740 ppm (-

180 190/+258 ppm) defines the remainder of the early Permian and coincides with multiple episodes of extensive and long-lived

volcanism (Fig. 2b; Torsvik et al., 2008; Zhai et al., 2013; Sato et al. 2015; Shellnutt, 2018; Chen and Xu, 2019). This pCO$_2$ rise is also coincident with a decline in O$_2$:CO$_2$ to below present-day values (Fig. 2b, S1b, 3a).

Short-term intervals of rising or falling CO$_2$ in the LOESS trend, within dating uncertainties, coincide with a brief but acute glaciation in the Kasimovian and with repeated deglaciations in south-central Gondwana in the early Permian (Griffis et al., 2018; Griffis et al., 2019), as well as with restructuring of marine and terrestrial ecosystems (Figs. 3b-d). The statistical significance of these short-term rises and falls in CO$_2$ was evaluated by analyzing the raw Monte Carlo estimates (10,000 model runs per data point shown on the LOESS trend) generated by the aforementioned CO$_2$ models (Breecker, 2013; Franks et al., 2014), from which the bootstrapped CO$_2$ estimates for eleven increments of short-term rise or fall were subsequently determined (Fig. 4a). The analysis of the Monte Carlo CO$_2$ estimates within these short-term intervals of rising or falling CO$_2$ indicates that 72.5 to 100% of the data confirm a visually observed increasing or decreasing trend (Fig. 4).

4 Discussion

4.1 Declining CO$_2$ through the Main Phase of the LPIA

Atmospheric CO$_2$ concentrations in the final 13 Myr of the Carboniferous (the Pennsylvanian portion of our record) are generally higher than those of the earliest Permian (Fig. 2b) and overall decline through the later part of the Carboniferous. Higher pCO$_2$ in the latter half of the Pennsylvanian is compatible with the hypothesized waning of large Early to Middle Pennsylvanian glaciers in the Late Pennsylvanian (c.f. Fielding et al., 2008), including widespread terminal deglaciation in a major glacial depocenter in south-central Gondwana (Parana Basin, Brazil) toward the close of the Carboniferous (Griffis et al., 2018; Griffis et al., 2019). Declining pCO$_2$ toward a nadir in the earliest Permian is also consistent with a renewed increase in the geographic distribution of glacial deposits in Gondwana beginning in the Late Pennsylvanian and peaking in the earliest Permian (Fig. 2b; Soreghan et al., 2019).

A tectonically driven increase in CO$_2$ consumption via a strengthening of the silicate weathering ('climate stabilizing') negative feedback (Walker et al., 1981; Berner and Caldeira, 1997) has been proposed as the driver of the Pennsylvanian decline in pCO$_2$ (Goddéris et al., 2017). The strength of the negative feedback varies with the degree of 'weatherability' (i.e., the susceptibility to weathering), which, in turn, is predominantly controlled by the intensity of the hydrologic cycle

206 (precipitation and surface runoff), with further influence by surface temperature and vascular plants (Dessert et al., 2001;

207 Donnadieu et al., 2004; West, 2012; Maher and Chamberlain, 2014; Caves et al., 2016; Ibarra et al., 2016). Uplift of the

208 Central Pangean Mountains (CPM) through the Pennsylvanian would have increased weatherability in the tropics by

209 inducing orographic precipitation and creating steeper slopes (Goddéris et al., 2017), thus providing a greater supply of fresh

210 mineral surfaces and enhanced surface runoff with longer fluid travel paths (cf. Maher and Chamberlain, 2014).

211 Consequently, CPM-induced increased weatherability and CO_2 consumption would have enhanced the global efficiency of

212 weathering and created a tighter coupling between CO_2 and climate at this time (cf. Maher and Chamberlain, 2014; Caves et

213 al., 2016).

214 The results of our GEOCLIM modeling, for a Himalayan-type mountain range (an analog for the CPM) and

215 parameterized such that 30% of the alkalinity generated by silicate weathering originates from the weathering of mafic rocks

216 (referred to as the 'reference continental silicate mineral assemblage or GEOCLIM_REG), indicates steady-state CO_2

217 concentrations (blue symbols and lines on Fig. 5A and B) that are well below the middle to late Carboniferous (340 to 300

218 Ma) threshold for initiation of continental ice sheets (840 ppm; Lowry et al., 2014). A hypothesized primary influence of the

219 CPM on CO_2 consumption through increased weatherability is further supported by the coincidence of modeled seawater and

220 marine proxy $^{87}Sr/^{86}Sr$ values that define a plateau of peak radiogenic values that is sustained for 15-Myr of the late

221 Carboniferous (318 to 303 Ma; Fig. 5b). The proxy-based seawater $^{87}Sr/^{86}Sr$ plateau has been long interpreted to record

222 exposure and weathering of uplifted and metamorphosed crustal rocks of the CPM that had radiogenic Sr isotope

223 compositions (Chen et al., 2018; Chen et al., in press). Additionally, the burial of substantial organic matter as peat in swamp

224 environments prone to preservation (ultimately as coal) during the Pennsylvanian would have partitioned global CO_2

225 consumption between silicate weathering and organic carbon burial, further driving steady-state pCO_2 lower (D'Antonio et

226 al., 2019; Ibarra et al., 2019). Our modeling, however, assumes a constant pre-Hercynian solid Earth degassing through the

227 study interval and does not account for increased magmatic CO_2 during Hercynian arc-continent collision and potential

228 widespread eruptive volcanism in the late Carboniferous (Soreghan et al., 2019), both of which could have increased steady-

229 state CO_2.

230 Short-term fluctuations in pCO_2 are superimposed on the long-term decline through the latter portion of the

9

Carboniferous. These short-term fluctuations have been confirmed as statistically significant (99.9 to 100% of estimates; Fig. 4b-d) and coincide with major environmental and biotic events. The brief interval of minimum pCO_2 (an average of ~300 ppm, but as low as 180 ppm) in the late Carboniferous (Kasimovian Stage, 307 to 304.5 Ma; Fig. 3b) coincides with a short-lived but acute glaciation (306.5 to 305 Ma) recorded by prominent valley incision and large-scale regression recorded by cyclothemic successions in the US Appalachian Basin and Midcontinent, as well as the Donets Basin, Ukraine (Belt et al., 2011; Eros et al., 2012; Montañez et al., 2016). Significant and repeated restructuring of wetland forests throughout tropical Euramerica, involving quantitative changes in floral composition and dominance, occurred during this 2.5 Myr pCO_2 minimum (and O_2:CO_2 maximum; Fig. 3a–c). Before the short-term pCO_2 low, Euramerican tropical forests had expanded to their maximum aerial extent ($\geq 2 \times 10^6$ km^2) under CO_2 concentrations of ~500 ppm (Moscovian Stage, Fig. 3b). The aerial extent of these forests dropped by half (green X in Fig. 3c; Cleal and Thomas, 2005) coincident with the decline in pCO_2 and near doubling of O_2:CO_2 (Fig. 3a–b). Moreover, within this pCO_2 low (Fig. 3b), arborescent lycopsids of the wetland forests went extinct throughout Euramerica (white X in Fig. 3c) and seasonally dry tropical floras shifted from cordaitalean- to walchian-dominance (~307–306.8 Ma; Fig. 3c; DiMichele et al., 2009; Falcon-Lang et al., 2018). These restructuring events occurred at or proximal to CO_2 falling below 400 ppm, supporting a previously hypothesized but untested CO_2 threshold for the Pennsylvanian ecologic turnovers (Fig. 3b–c; Beerling et al., 1998; Beerling and Berner, 2000; Montañez et al., 2016). In the oceans, foraminiferal diversity decreased substantially during the Kasimovian pCO_2 low with the loss of ~200 species (~58% of all taxa; first gray bar in Fig. 3d; Groves and Yue, 2009) presumably due to decreasing seawater temperatures.

The interval of CO_2 minima was terminated by a rapid rise across the Kasimovian-Gzhelian boundary (303.7 Ma) to CO_2 concentrations above 600 ppm (Fig. 2b; S1b). The short-term interval of elevated pCO_2 (304 to 302.5 Ma) is coincident with a ~1.5‰ decline in seawater $\delta^{13}C$ (Grossman et al., 2008; Chen et al., in press), compatible with a decline in the CO_2 sink provided by terrestrial organic C (peats) burial (gray bar on Fig. 2b) and/or a peak in pyroclastic volcanism between ~310 and 301 Ma (Soreghan et al., 2019). This period of increased pCO_2 overlaps with the Alykaevo Climatic Optimum (orange bar on Fig. 3c), defined by the invasion of tropical Euramerican vegetation into the *Rufloria*-dominated, mid-latitude Angaran floral province (Cleal and Thomas, 2005). Terminal deglaciation in south-central Gondwana (Parana Basin, Brazil), U-Pb dated to between ~302 and 298 Ma (Cagliari et al., 2016; Griffis et al., 2018), may have been linked to the Late

256   Pennsylvanian interval of elevated CO_2, although this requires further testing (Figs. 2b, 3b). Conversely to the Kasimovian

257   CO_2 low, a significant change in global diversity of foraminifera involving a doubling of species occurred during this

258   subsequent period of elevated CO_2 and presumed increase in seawater temperatures (black bar on Fig. 3d; Groves and Yue,

259   2009).

260

261   **4.2 An Early Permian CO_2 Nadir**

262   Atmospheric pCO_2 dropped substantially across the Carboniferous-Permian Boundary (i.e., 298.9 Ma) to a 10-Myr interval

263   (300–290 Ma) of the lowest concentrations (175 to <400 ppm) of the 40-Myr record (Fig. 2b). The CO_2 nadir, which spans

264   the Asselian and Sakmarian stages, coincides with renewed glaciation and maximum ice sheet extent, marking the apex of

265   LPIA glaciation (Fig. 2b; Fielding et al., 2008; Isbell et al., 2012; Montañez and Poulsen, 2013; Soreghan et al., 2019), as

266   well as with a large magnitude eustatic fall archived in paleotropical successions worldwide (Koch and Frank, 2011; Eros et

267   al., 2012). Widespread glacial expansion temporally linked to this interval of lowest overall pCO_2 argues for CO_2 as the

268   primary driver of glaciation rather than recently proposed mechanisms, such as the influence of the closing of the Precaspian

269   Isthmus (Davydov, 2018) or a decrease in the radiative forcing resulting from increased atmospheric aerosols by explosion

270   volcanism at this time (Soreghan et al., 2019). The very low greenhouse radiative forcing associated with this low CO_2

271   interval would have been amplified by 2.5% lower solar luminosity (Crowley and Baum, 1992), reduced transmission of

272   short-wave radiation (Poulsen et al., 2015) by the high pO_2 atmosphere of the early Permian (Krause et al., 2018; Lenton et

273   al., 2018), and by increased atmospheric aerosols at this time (Soreghan et al., 2019).

274   The 10-Myr pCO_2 nadir raises a paradox as to what was the primary CO_2 sink(s) at the time given that the CO_2 sinks of

275   the Pennsylvanian were no longer prevalent. This paradox reflects the waning denudation rates of the CPM by the early

276   Permian (Goddéris et al., 2017), intensifying pantropical aridification, possibly driven by increasing continentality (yellow to

277   red bar in Fig. 3c; DiMichele et al., 2009; Tabor et al., 2013), and the demise of the wetland tropical forests and associated

278   loss of peats before the close of the Carboniferous (black-to-gray bar in Fig. 2b; Hibbett et al., 2016). In turn, surface runoff

279   would have been inhibited and the supply of fresh silicate minerals decreased, thus lowering overall weatherability.

280   Atmospheric CO_2 under the influence of these environmental factors should have equilibrated in the earliest Permian at a

281   new higher steady-state level, even if solid Earth degassing did not increase (cf. Gibbs et al., 1999), thus raising a paradox. If

282 volcanism was increasing by this time (Fig. 2b and associated references; Soreghan et al., 2019), then this paradox is even

283 greater.

284 Two mechanisms have the potential to resolve this paradox. The first, referred to as a delayed climate-controlled

285 capacitor (Joshi et al. 2019), leads to a multi-million-year delay between the timing of peak orogenic uplift and maximum

286 chemical weathering potential and CO_2 drawdown due to substantial differences in chemical weathering rates during the

287 different phases of an orogenic cycle. In their study, the highest intensity of chemical weathering and capacity for CO_2

288 consumption occurs when mountains have been somewhat denuded rather than during peak uplift, reflecting the

289 disproportionate influence of runoff temperature over hydrology and erosion on weathering potential. Notably, Joshi et al.'s

290 (2019) coupled climate and geochemical modeling of the Late Paleozoic Ice Age yield an evolution of simulated pCO_2 over

291 the period of uplift and denudation of the CPM that corresponds both in absolute CO_2 concentrations and magnitude of

292 change over this period (~320 to 290 Ma). That said, in Joshi et al. (2019), the physical erosion parameter is not dependent

293 on climate, but, rather, is defined by the prescribed altitude. Thus, physical erosion is an external forcing in their model. The

294 absence of runoff dependence for physical erosion (as is the case for GEOCLIM) and the strong dependence of weathering

295 on temperature may be the trigger for their simulated delay between maximum uplift and the highest intensity of CO_2

296 consumption by silicate weathering. In GEOCLIM, the dependence of the physical erosion on runoff does not allow for

297 millions of years delay between maximum uplift of the CPM and lowest simulated pCO_2. Further study is needed to

298 interrogate the influence of this approach on the results.

299 The second mechanism, proposed here, is a substantial shift in the ratio of mafic-to-granite rocks available for

300 weathering from the latest Carboniferous to the early Permian. This reflects the doubling or greater increase in weatherability

301 of mafic mineral assemblages over granitic assemblages (Gaillardet et al., 1999; Dessert et al., 2003; Ibarra et al., 2016), thus

302 enhancing weathering efficiency and CO_2 drawdown and creating a tighter coupling between CO_2 and climate. In turn, with

303 tighter coupling between CO_2 and climate, the global silicate weathering flux needed to maintain homeostatic balance in the

304 carbon cycle for a given scenario can be attained at a lower pCO_2 level.

305 Macdonald and others (2019) hypothesized that increased weatherability provided by the exhumation of ophiolites

306 along the ~10,000 km long Hercynian arc-continent suture zone, primarily situated in the paleotropics, was capable of

lowering pCO_2 below the ice initiation threshold in the Carboniferous (i.e., Pennsylvanian), thus instigating the Late Paleozoic Ice Age. Here, we used the GEOCLIM model to, first, interrogate this Carboniferous hypothesis further and, second, to evaluate the potential of increased weatherability, provided by increasing the ratio of outcropping mafic rocks to granite rocks available for weathering, as the predominant driver of the early Permian CO_2 nadir. Figure 5 illustrates the influence of a successive increase in the surface area of outcropping mafic rocks beginning with the reference continental silicate mineral assemblage (GEOCLIM-REG), which was used to evaluate the influence of Pennsylvanian uplift of the CPM, to an up to 4-fold increase in the outcropping of mafic rocks. In the GEOCLIM context, the weathering of mafic rocks is dependent on the surface of each grid cell, and on the associated local runoff and air temperature, multiplied by a calibration constant. Increasing the exposure area of mafic rocks is mathematically equivalent to multiplying the calibration constant.

Between 300 and 290 Ma, when predominant Pennsylvanian CO_2 sinks were lost (terrestrial organic C burial) or waning (decreased precipitation and denudation rates of the CPM), modeled steady-state atmospheric CO_2 is maintained at or below the CO_2 threshold for initiation of continental ice sheets (560 ppm; Lowry et al., 2014) when the surface area of outcropping mafic rocks is greater than 2-fold that of GEOCLIM-REG (Fig. 5a). Conversely, steady-state CO_2 rises well above the glacial threshold (to 3500 pm) for the 'reference' continental silicate rock assemblage (Fig. 5a). Although volcanism remained geographically extensive through the 10-Myr CO_2 nadir (Soreghan et al., 2019), the impact on atmospheric CO_2 would have been short-lived ($\leq 10^5$ kyr; Lee and Dee, 2019), and eclipsed on the longer term by the increased weatherability provided by increased exposure of mafic rocks along the Hercynian arc-continent suture zone, lowering steady-state CO_2 to, potentially, pre-volcanism levels (cf. Dessert et al., 2001).

Independent evidence for a substantial shift in the partitioning of silicate weathering to more mafic mineral assemblages in the earliest Permian exists in the late Paleozoic proxy-based seawater Sr isotope record, which documents a rapid (0.000043/Myr) and near-linear decrease in seawater $^{87}Sr/^{86}Sr$ beginning in the latest Carboniferous (~303 Ma) and continuing into the middle Permian (Fig. 5b; Chen et al., in press). The simulated trends in seawater $^{87}Sr/^{86}Sr$ for GEOCLIM-REG (blue line on Fig. 5b) through a 2- to 4-fold increase in the area of exposed mafic rocks capture the rapid rise through the upper Carboniferous to peak values in the latter half of the Pennsylvanian and subsequent decline through the early

13

332 Permian. The rapid rate of decline in proxy $^{87}Sr/^{86}Sr$ values post-300 Ma, however, is best bracketed by simulated $^{87}Sr/^{86}Sr$

333 for a 2- to 4-fold increase in mafic rock exposure. Moreover, the best fit of the simulated trends to the geochronologically

334 well-constrained bioapatite data (blue and green crosses on Fig. 5b) suggests a progressive increase in mafic-to-granite ratio

335 through the 10-Myr CO_2 nadir. This finding, together with the hypothesized need (the aforementioned mechanism two) for

336 minimally a 4-fold increase in mafic-rock outcropping in order to maintain CO_2 concentrations below the ice initiation

337 threshold for a sustained period longer than that of hysteresis (i.e., throughout the interval of minimum CO_2 and apex of

338 glaciation; Fig. 5), argues for a substantial increase in weatherability from the Carboniferous to early Permian driven by a

339 compositional shift in outcropping rocks available for weathering to a higher mafic-to-granite ratio.

340   If peak ophiolite exhumation and maximum CO_2 consumption by their weathering occurred in the late Carboniferous,

341 thus initiating the LPIA (~330 to 300 Ma) as has been suggested (Table S1 of Macdonald et al., 2019), then our modeling

342 results suggest that a substantial increase in solid Earth degassing rate at this time would have been necessary. In our

343 simulation, increasing the surface area of outcropping mafic rocks (2- to 4-fold) during the Pennsylvanian results in steady-

344 state atmospheric CO_2 levels approaching Snowball Earth conditions given other operating influences on weatherability and

345 CO_2 sequestration at the time and no change in degassing rate (Fig. S6). Such conditions are not compatible with proxy

346 inferred moderate surface conditions of the late Carboniferous (Montañez and Poulsen, 2013) and the radiation of forest

347 ecosystems throughout the tropics (DiMichele, 2014). Rather, we hypothesize that the sustained CO_2 nadir and expansion of

348 ice sheets in the first 10 Myr of the Permian record a major reorganization of the predominant factors influencing

349 weatherability in the tropics across the Carboniferous-Permian transition, in particular, a substantial shift in the ratio of

350 mafic-to-granitic rocks available for weathering.

351   Similar to the short-term fluctuations superimposed on the later Carboniferous long-term decline in CO_2, two

352 statistically significant (94 to 100% on Fig. 4e–h) short-term increases in pCO_2 are superimposed on the early Permian nadir

353 (Fig. 3b). The first (298 to 296 Ma) coincides, within age uncertainty, with a major deglaciation event in the Karoo (southern

354 Africa) and Kalahari (Namibia) basins of south-central Gondwana (296.41 Ma +0.27/-0.35 Ma; Griffis et al., 2019). The

355 second short-term rise in pCO_2 (294.5 to 292.5 Ma) overlaps with the onset of widespread ice loss in several southern

356 Gondwanan ice centers (Fig. 2b; Soreghan et al., 2019). This CO_2-deglaciation link suggests that continental ice stability in

14

357 the early Permian dropped substantially when pCO_2 rose above ~ 300 to 400 ppm and thus raises the question as to whether

358 the ice sheet CO_2 threshold was even lower than modeled (560 ppm; Lowry et al. 2014) during the earliest Permian.

359   Notably, the early Permian pCO_2 minimum (Fig. 2b, S1b) and associated anomalously high $O_2:CO_2$ (700 to 960; Fig.

360 3a) is an interval of major ecosystem changes. The geologically rapid and large-magnitude drop in pCO_2 prior to and across

361 the Carboniferous-Permian boundary interval (Fig. 2b, S1b) coincides with a permanent shift in plant dominance from

362 swamp-community floras to seasonally dry vegetation (Black X on Fig. 3c). That shift in plant dominance has been long

363 attributed to intensification of an aridification trend that began in the mid-Pennsylvanian (yellow to red bar in Fig. 3c;

364 DiMichele et al., 2009; Tabor et al., 2013). Analogous to the vegetation turnover and extinction during the Pennsylvanian

365 CO_2 minimum, this permanent shift to seasonally dry vegetation is coincident with the earliest Permian drop in pCO_2 to

366 concentrations below 400 ppm, suggesting a possible ecophysiological advantage of these plants over the wetland floral

367 dominants that they replaced (Fig. 3a–c; c.f., Wilson et al., 2017). The high water use efficiency of the seasonally dry plants

368 would have made them water stress-tolerant and, in turn, would have amplified aridification through a modeled ~50%

369 decrease in canopy-scale transpiration (Wilson et al., 2017; Wilson et al., 2020). The extreme habitat restriction of wetland

370 floras was particularly consequential for tetrapods, leading to the acquisition of terrestrial adaptions in crown tetrapods and

371 the radiation and eventual dominance of dryland-adapted amniotes, possibly, shaping the phylogeny of modern terrestrial

372 vertebrates (Fig. 3c; Pardo et al., 2019).

373   Moreover, the CO_2 decline at the Carboniferous-Permian boundary into the 10-Myr nadir and associated peak in

374 $O_2:CO_2$ also corresponds to the evolution and radiation of glossopterids and gigantopterids (McLoughlin, 2011; Zhou et al.,

375 2017), with increasing vein density in the former (Fig. 3a–c; Srivastava, 1991). These plant groups had complex,

376 angiosperm-like venation (Melville, 1983; Srivastava, 1991), with gigantopterids having the only known pre-Cretaceous

377 vessels in their stems (Li et al., 1996). The increased hydraulic capacity provided by these morphological characteristics

378 would have conferred a significant ecological advantage to these plants under the low CO_2, high O_2, and elevated aridity

379 conditions in which they evolved (cf. Gerhart and Ward, 2010; de Boer et al., 2016). In the oceans, a marked collapse in

380 foraminiferal diversity with a notable fall in species to a minimum from a Pennsylvanian zenith (425 to 110 species; Fig. 3d,

381 e; Groves and Yue, 2009) spanned the 10-Myr pCO_2 nadir, analogous to the diversity drop during the Pennsylvanian low

382   CO_2 interval.

383

384   **4.3 CO_2-Forced Demise of the LPIA**

385   The 10-Myr CO_2 nadir terminated at 290 Ma with the onset of a protracted CO_2 rise that persisted to the highest levels of the

386   record (~740 ppm [-190/+258]) by the close of the early Permian (Fig. 2b). The onset of this protracted CO_2 rise overlaps

387   with initiation of a period of large-magnitude magmatism (red bars in Fig. 2b). Widespread volcanism began around 297.4

388   Ma (± 3.8 Ma) in northern Europe (Skagerrak-centered Large Igneous Province), extending well into Germany (Rotliegend)

389   (Torsvik et al., 2008; Käßner et al., 2019). The multi-stage Tarim magmatic episodes in China (292–272 Ma; with peaks at

390   ~290 Ma and 280 Ma; Fig. 2b; Chen and Xu, 2019), was likely associated with large magnitude CO_2 emissions given that

391   the magma, which distributed basalt (400 m thick) over a 2.5×10^5 km^2 region (Yang et al., 2013), intruded a thick

392   succession of early Paleozoic marine carbonates (Gao et al., 2017). The Panjal Traps, NW India (289 Ma ± 3 Ma; Shellnutt,

393   2018) and the compositionally similar Qiangtang Dykes (283 Ma ± 2 Ma; Fig. 2b; Zhai et al., 2013), albeit relatively small in

394   extent, were an additional potential volcanic CO_2 source, along with contemporaneous volcanism in Oman. Furthermore,

395   protracted Choiyoi volcanism, which began at 286.5 Ma ± 2.3 Ma (Sato et al., 2015) and continued over ~39 Myr in western

396   Argentina, may have contributed substantial pulses of greenhouse gases in the early Permian (Spalletti and Limarino, 2017).

397   Once each magmatic episode waned, however, the mafic-dominated magmatic deposits would have served as longer-term

398   regional sinks leading to increased global CO_2 consumption (cf. Lee et al., 2015). Thus, for steady-state CO_2 to have

399   increased through the remainder of the early Permian, the relative influence of CO_2 inputs must have outpaced that of these,

400   and other, outputs (CO_2 sinks).

401   Our modeled (GEOCLIM) steady-state CO_2 for a 4-fold increase in outcropping of mafic rocks surpasses the ice-sheet

402   initiation threshold at the termination of the CO_2 nadir (~290 Ma; red line and symbols on Fig. 5a), despite no change in

403   solid Earth degassing. That low CO_2 concentrations could no longer be maintained, despite a 4-fold increase in mafic rock

404   exposure, reflects overall intensifying aridification, denudation of the CPM, and a shift from dense forests to savanna-like

405   vegetation in Euramerica at this time. However, given that the magmatic CO_2 flux likely increased already by the earliest

406   Permian (summarized on Fig. 2b), our model results indicate that maintaining low steady-state CO_2 concentrations during

407   the earliest Permian 10-Myr CO_2 nadir would have required an increasingly greater proportion of mafic rock weathering over

408   the reference continental silicate mineral assemblage of the Pennsylvanian, possibly well beyond a 4-fold increase.

409   A CO_2-forced demise of the Late Paleozoic ice age after 290 Ma is supported by the loss of continental ice from the

410   main ice depocenters in south-central Gondwana by 282.17 +0.32/-0.44 Ma (Griffis et al., 2018; 2019) and a 6-fold drop in

411   documented glacial deposits overall between the Sakmarian and Artinskian stages (Fig. 2b; Soreghan et al., 2019). The long-

412   term CO_2 rise through the remainder of the early Permian coincided with substantial marine and terrestrial ecosystem

413   perturbation (Fig. 3b–d; Chen and Xu, 2019). In the marine biosphere, the uniformly low rates of global macroevolution in

414   marine organisms (brown bar on Fig. 3d) were reversed and broadly adapted and distributed genera reappeared, thus

415   restoring marine ecosystems to their pre-LPIA rates (Stanley and Powell, 2003). Pennsylvanian rugose corals (pink bar on

416   Fig. 3d) underwent a major turnover in composition to those that dominated until the End-Permian extinction and cold-

417   adapted marine bivalves and brachiopods turned over to warm-adapted forms synchronous with the onset of the long-term

418   increase in $p$$CO_2$ (290.1 Ma; blue to red bar across the Sakmarian-Artinskian boundary on Fig. 3d; Wang et al., 2006;

419   Clapham and James, 2008). On land, the loss of pelycosaur families (three in the late Artinskian and four in the early

420   Kungurian (Kemp, 2006) coincided with CO_2 sustained at >500 ppm. By the close of the Kungurian and the time of highest

421   CO_2 (740 ppm), basal synapsids largely disappeared and were replaced by more derived therapsids, tetrapod diversity

422   decreased significantly (Benton, 2012; McGhee, 2018), plant extinction rates reached a level comparable to that associated

423   with the extinction of arborescent lycopsids in the early Kasimovian (Cascales-Miñana et al., 2016), and

424   extinction/origination rates increased in fishes (Friedman and Sallan, 2012).

425

426   **5 Conclusions**

427   Glacial-interglacial climate cycles and large-scale glacioeustasy, as well as repeated ecosystem change analogous to that of

428   the Pleistocene, characterized Earth's penultimate icehouse in the late Paleozoic. The dynamic glaciation history of this

429   icehouse (the Late Paleozoic Ice Age (LPIA)) came to a close by the end of the early Permian with turnover to permanent

430   greenhouse conditions. Thus, improved constraints on how atmospheric $p$$CO_2$ evolved during the LPIA and its subsequent

431   demise is crucial for better understanding the role of greenhouse-gas forcing on Earth System processes during this time. The

432 new and age-recalibrated pCO_2 reconstruction presented here for a 40-Myr interval (~313 to 273 Ma) of the late Paleozoic

433 substantially refines existing Permian CO_2 estimates and provides perhaps the highest temporal resolution protracted pCO_2

434 record prior to the Cenozoic. The multiproxy record confirms the previously hypothesized CO_2-glaciation linkage, including

435 documenting the coincidence of a 10-Myr period of minimum pCO_2 with inferred maximum ice extent during the earliest

436 Permian. A long-term decline in pCO_2 through the late Carboniferous period of glaciation, culminating in the earliest

437 Permian CO_2 nadir, lends support for a previously modeled progressive decrease in the CO_2 threshold for continental ice

438 sheets through the LPIA.

439   Our new pCO_2 record provides the first stomatal-based evidence for elevated (up to 700 ppm) atmospheric CO_2

440 concentrations during short-term (10^4-yr) interglacials. Together with new O_2:CO_2 estimates of similar temporal resolution to

441 pCO_2, the new atmospheric trends indicate a close temporal relationship to repeated ecosystem restructuring in the terrestrial

442 and marine realms. In terrestrial ecosystems, the appearance and/or rise to dominance of plants with physiological and

443 anatomical mechanisms for coping with CO_2 starvation and marked aridity correspond to drops in CO_2 below 400 ppm (as

444 low as ~180 ppm) and O_2:CO_2 ratios nearly double those of late Paleozoic background values. Similarly, decreasing rates of

445 macroevolution and diversity in the low-latitude oceans correspond to falling CO_2 to below 400 ppm. These CO_2–ecosystem

446 relationships lead us to hypothesize that 400 ppm was an important threshold for ecosystem resilience during the late

447 Paleozoic.

448   Modeling of steady-state pCO_2 during the late Paleozoic using an intermediate complexity climate-carbon cycle model

449 (GEOCLIM) and comparison to the new multi-proxy CO_2 record provides new insight into the relative influences of uplift of

450 the Central Pangean Mountains, intensifying aridification, and increasing mafic to-granite rock ratio of outcropping rocks on

451 the global efficiency of CO_2 consumption and secular change in steady-state pCO_2 through the late Paleozoic. The

452 simulations confirm that, for the Carboniferous, enhanced weatherability and CO_2 consumption provided by the influence of

453 uplift on surface hydrology and erosion could have lowered atmospheric pCO_2 well below the threshold for ice sheet

454 initiation. Increasing the availability of mafic rocks for weathering drives CO_2 levels toward snowball Earth conditions in the

455 Carboniferous. Conversely, a substantial increase (up to 4-fold) in the surface outcropping of mafic rocks over those

456 modeled for the Carboniferous is needed to maintain the 10-Myr CO_2 nadir in the earliest Permian and is compatible with

18

457   maximum exhumation of the Hercynian orogenic belt at this time as well as with a rapid decline in proxy-based seawater

458   [87]Sr/[86]Sr. Although these findings support the hypothesis of atmospheric pCO$_2$ response to uplift of the CPM as the primary

459   driver for Carboniferous initiation of the LPIA (Goddéris et al., 2017), they argue for a major reorganization of the

460   predominant surface factors influencing weatherability in the tropics across the Carboniferous-Permian in order for pCO$_2$ to

461   values to have fallen to well below 300 ppm. The demise of the LPIA was greenhouse gas-forced, reflecting the increasing

462   importance of magmatic degassing and likely decreased weathering efficiency driven by intensifying aridification,

463   denudation of the CPM, and the loss of the wetland forests throughout tropical Euramerica.

464   **Figures**
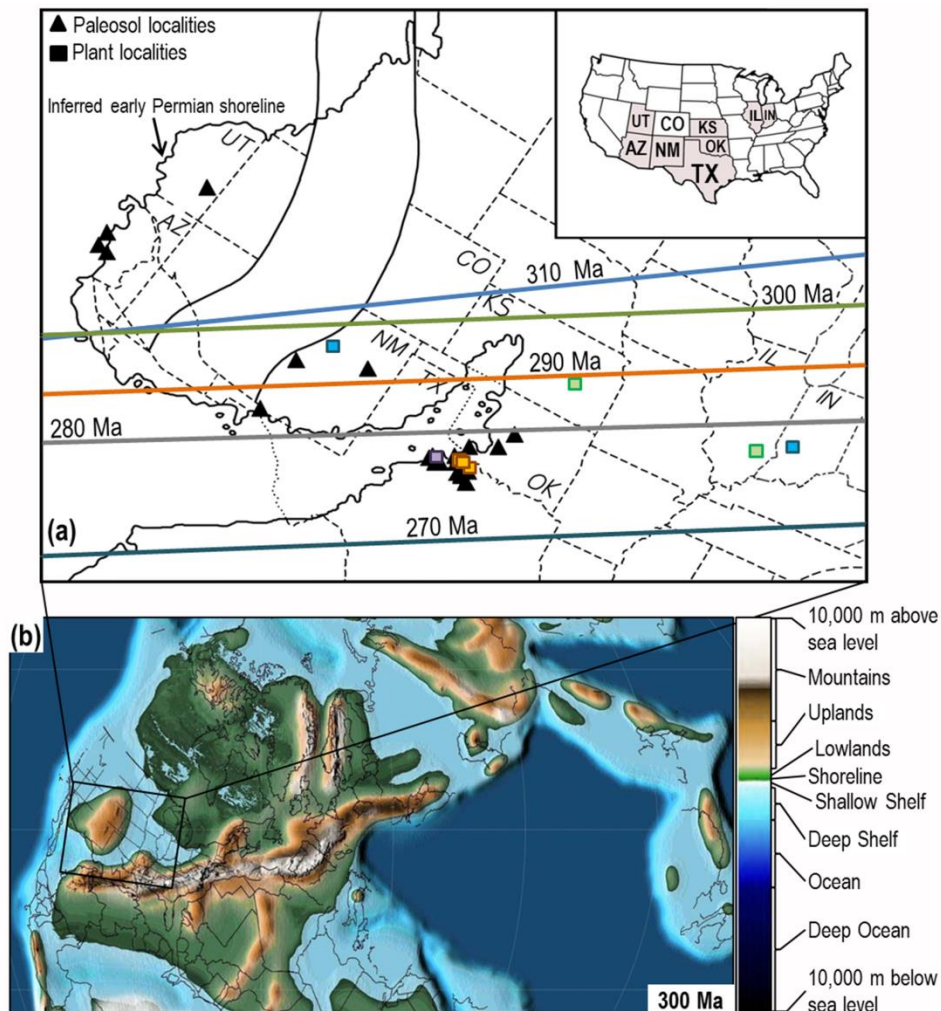
465

466 **Figure 1: Sampling localities in present-day and late Paleozoic geographic context**. **(a)** Sampling locations of pedogenic

467 carbonates and plant fossils and their position relative to the Late Pennsylvanian (310 & 300 Ma) and early Permian (290 to

468 270 Ma) equator (the colors of the flora localities correspond to that of the paleo-equator at that time). White band traversing

469 NM and CO is the area of inferred shortening during the Laramide and Sevier orogenies. Map modified from Montañez et

470 al., (2007). **(b)** Earliest Permian (290 Ma) paleogeography (Scotese, 2016); shading corresponds to paleo-

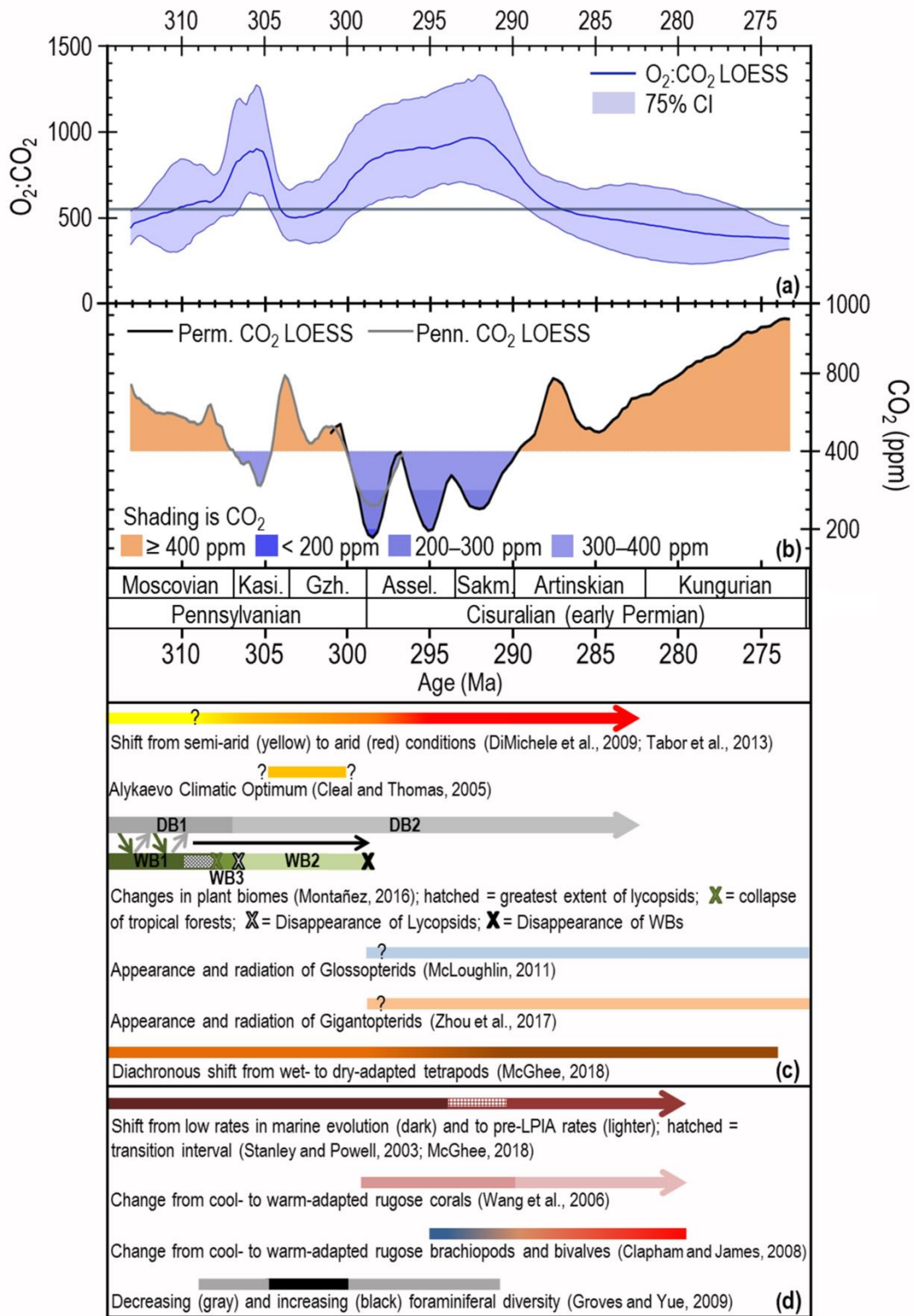471 topographic/bathymetric scale on the right. Inset box is the location of panel (a).

472

473
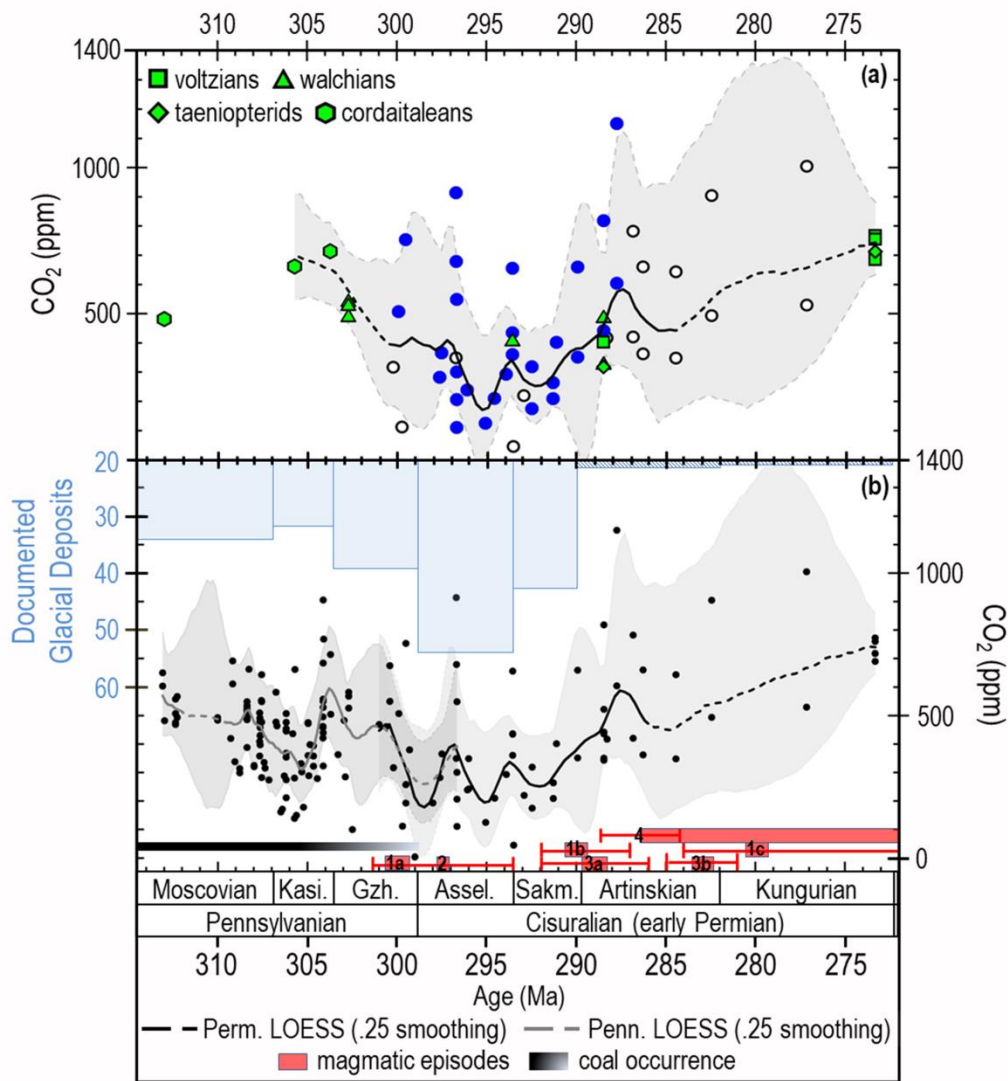
Figure 2: Late Paleozoic CO₂ estimates. **(a)** New and revised (Montañez et al., 2007) pCO_2 estimates, bootstrapped LOESS trend, and 75% confidence interval (CI). Revised pedogenic carbonate-based estimates were made using $\delta^{13}C_{OOM}$ (blue filled circles; n = 28; Fig. S1) and $\delta^{13}C_{POM}$ (open black circles; n = 16; Fig. S1). Trendline is the median of 1000 bootstrapped LOESS analyses; dashed intervals indicate low data density and higher uncertainty. See Material and Methods for details, Fig. S1 for error bars on individual CO_2 estimates and the 95% CI, and Richey et al. (2020; https://doi.org/10.25338/B8S90Q for the full dataset. **(b)** Multiproxy CO_2 record and individual estimates (this study and age-recalibrated values of Montañez et al., (2016); n = 165), documented glacial deposits (Soreghan et al., 2019), and best

21

482   estimate of timing (and uncertainties) of magmatic episodes: 1a = Tarim 1, China (~300 Ma); 1b = Tarim 2 (292–287, peak

483   ~290 Ma); 1c = Tarim 3 (284–272, peak ~ 280 Ma; Chen and Xu, (2019)); 2 = Skagerrak-centered, NW Europe (297.5 ± 3.8

484   Ma; Torsvik et al., (2008)); 3a = Panjal Traps, NW India (289 ± 3 Ma; Shellnutt, (2018)); 3b = Qiangtang Traps, Tibet (283

485   ± 2 Ma; Zhai et al., (2013)); 4 = Choiyoi, W Argentina (beginning 286.5 Ma ± 2.3 Ma, continuing for up to 39 Myr; Sato et

486   al., (2015)). Trendlines as in (A); dashed intervals across the Carboniferous-Permian boundary (298.9 Ma) indicates overlap

487   of the two LOESS trendlines.

488

489

310 305 300 295 290 285 280 275

O$_2$:CO$_2$

1500

1000

500

0

O$_2$:CO$_2$ LOESS
75% CI

(a)

Perm. CO$_2$ LOESS   Penn. CO$_2$ LOESS

1000

800

600

400

200

CO$_2$ (ppm)

Shading is CO$_2$
≥ 400 ppm   < 200 ppm   200–300 ppm   300–400 ppm

(b)

| Moscovian | Kasi. | Gzh. | Assel. | Sakm | Artinskian | Kungurian |

| Pennsylvanian | Cisuralian (early Permian) |

310   305   300   295   290   285   280   275

Age (Ma)

?

Shift from semi-arid (yellow) to arid (red) conditions (DiMichele et al., 2009; Tabor et al., 2013)

?   ?

Alykaevo Climatic Optimum (Cleal and Thomas, 2005)

DB1   DB2

WB1   WB3   WB2   X

Changes in plant biomes (Montañez, 2016); hatched = greatest extent of lycopsids; X = collapse of tropical forests; 𝕏 = Disappearance of Lycopsids; X = Disappearance of WBs

?

Appearance and radiation of Glossopterids (McLoughlin, 2011)

?

Appearance and radiation of Gigantopterids (Zhou et al., 2017)

Diachronous shift from wet- to dry-adapted tetrapods (McGhee, 2018)   (c)

Shift from low rates in marine evolution (dark) and to pre-LPIA rates (lighter); hatched = transition interval (Stanley and Powell, 2003; McGhee, 2018)

Change from cool- to warm-adapted rugose corals (Wang et al., 2006)

Change from cool- to warm-adapted rugose brachiopods and bivalves (Clapham and James, 2008)

Decreasing (gray) and increasing (black) foraminiferal diversity (Groves and Yue, 2009)   (d)

490

23

Figure 3: Late Paleozoic O$_2$:CO$_2$ and pCO$_2$, and comparison to environmental and biotic events. (a) O$_2$:CO$_2$ estimates using CO$_2$ values of this study and averaged time-equivalent modeled O$_2$ (Krause et al., 2018; Lenton et al., 2018). Trendline is the median of 1000 bootstrapped LOESS analyses; gray horizontal line is present-day O$_2$:CO$_2$. **(b)** Bootstrapped Pennsylvanian and Permian LOESS analyses (From Fig. 2A), with significant overlap across the Pennsylvanian- Permian boundary interval. The shading indicates CO$_2$ above (orange) and below (shades of blue) the mean value for the 16-million-year record through the late Pennsylvanian reported in Montañez et al., (2016). Temporal changes in terrestrial (c) and marine (d) ecosystems. Plant biomes from Montañez (2016): Wetland Biome (WB) 1 (i.e., lycopsid-dominated), WB 2 (i.e., cordaitalean/lycopsid co-dominance), WB 3 (i.e., tree fern-dominated), Dryland Biome (DB) 1 (i.e., cordaitalean-dominated), DB 2 (i.e., walchian-dominated). Diagonal arrows indicate 10^5-yr glacial-interglacial shifts between wet- and dry-adapted floras.
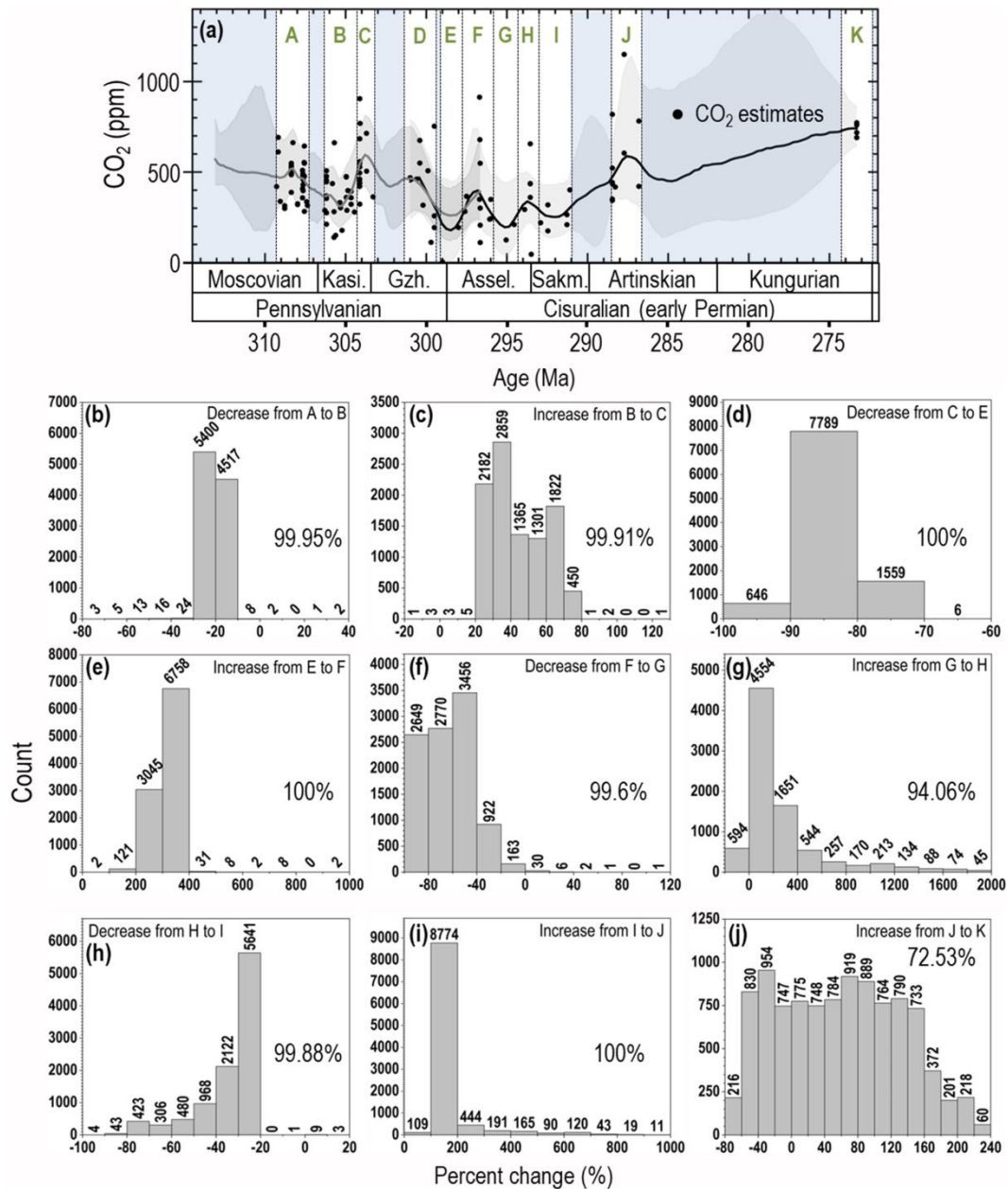
Figure 4: Analysis of the statistical significance of short-term CO₂ fluctuations. (a) White intervals (A–K) delineate short-term highs/lows in the CO₂ LOESS trend used for binning (n=11; bins ±0.5 to 1 Myr resolution). Raw stomatal- and pedogenic carbonate-based CO₂ estimates generated by Monte Carlo analysis (10,000 model runs per CO₂ estimate; data in shaded intervals were not used). CO₂ between bins was compared by calculating the mean of the lowest through 10,000th

506   (highest) Monte Carlo values for all CO_2 points in each bin and comparing the means of the two bins sequentially. **(b)–(h)**

507   Histograms of the percent change between each of the 10,000 Monte Carlo means of the adjacent bins. Negative values

508   indicate a decrease in value between bins, positive values, an increase. The number above each histogram bar is of the

509   'percent change' values represented in each bar. The percent of the 10,000 model runs that confirm a given increase or

510   decrease in the LOESS trend is indicated by the % value shown on the right side of each panel. See Materials and Methods

511   for further details.

512

513

514

515

516

517

518

519

520

521
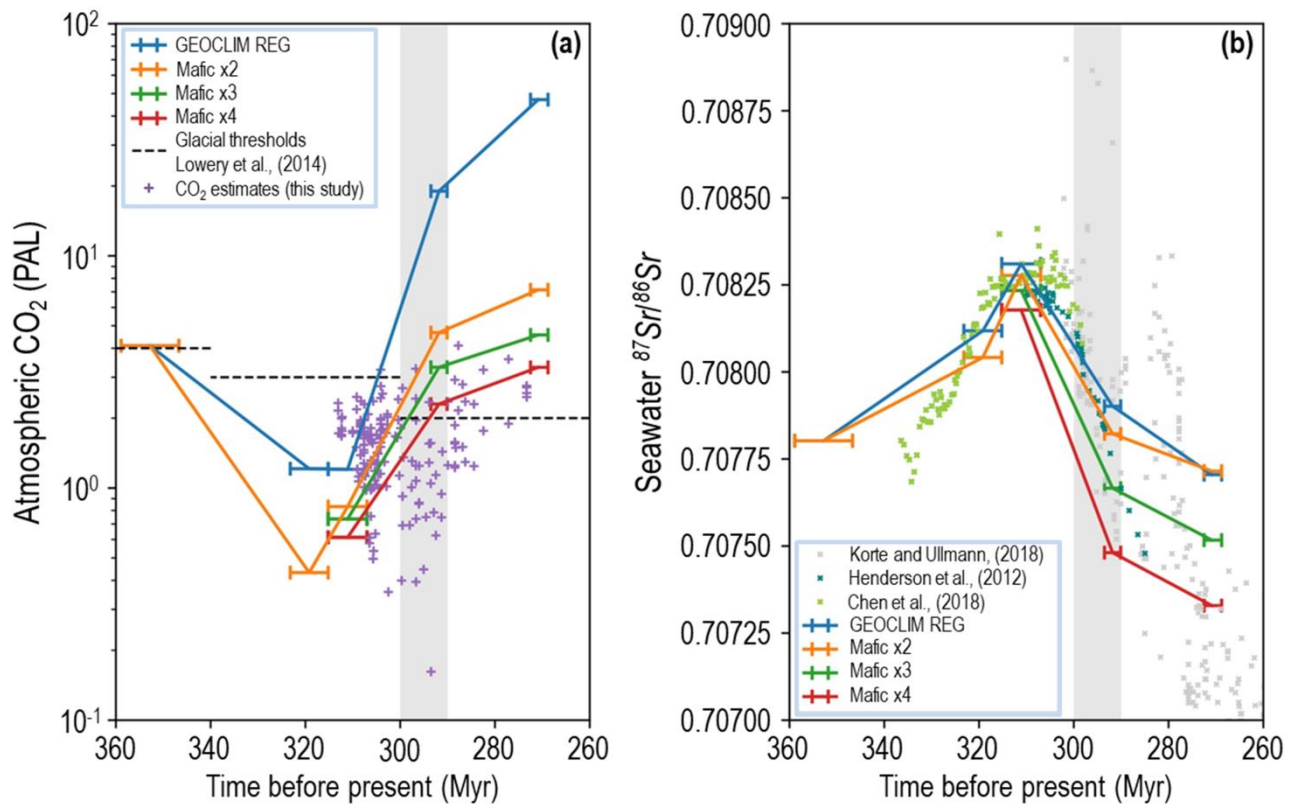
Figure 5: Carboniferous through early Permian modeled (GEOCLIM) steady-state atmospheric CO_2 and seawater $^{87}Sr/^{86}Sr$ for different surface areas of mafic rocks available for silicate weathering. In the model, maximum geographic extent and altitude (5000 m) of the CPM is reached in the Moscovian (320 Ma), with altitude decreasing to 3000 m at 290 Ma and 2000 m at 270 Ma. **(a)** Simulated (color lines) and proxy pCO_2 estimates (purple crosses, this study). Horizontal error bars on the colored lines represent the temporal uncertainty for simulated pCO_2 estimates. CO_2 thresholds for continental ice sheet initiation (360–340 Ma = 1120 ppm; 340–300 Ma = 840 ppm; 300–260 Ma = 560 ppm from Lowry et al., 2014) decrease in response to equatorward drift of Gondwana, favoring an overall reduction in ice-sheet size through time. The 'reference' surface area of outcropping mafic rocks (GEOCLIM REG) maintains steady-state atmospheric CO_2 below the ice initiation threshold from 350 to ~304 Ma. Steady-state atmospheric CO_2 for a 2-fold, 3-fold, and 4-fold increase in outcropping area of mafic rocks remains below the ice initiation threshold (560 ppm) up to ~300 Ma, crossing over at progressively later times in the early Permian. Threshold cross-over of steady-state CO_2 at ~290 Ma for a 4-fold increase in mafic rock exposure coincides with the termination of the 10-Myr CO_2 nadir (gray vertical bar; both panels). **(b)**

27

534 Seawater $^{87}Sr/^{86}Sr$ modeled for the same set of varying surface areas of outcropping mafic rocks and $^{87}Sr/^{86}Sr$ values of well-

535 preserved biogenic calcites (gray filled squares) and conodont bioapatites (green and blue filled squares). Horizontal error

536 bars on the colored lines represent the temporal uncertainty for modeled Seawater $^{87}Sr/^{86}Sr$.

537

538 **Data Availability**

539 Underlying primary data is deposited in the Dryad Digital Repository (Richey et al., 2020) and can be accessed at

540 https://doi.org/10.25338/B8S90Q.

541

542 **Author contribution**

543 JDR and IPM designed the study. JDR collected the data, wrote the manuscript, and drafted the figures; IPM and YG carried

544 out the GEOCLIM modeling, wrote relevant parts of the manuscript, and drafted Fig. 5. All co-authors provided comments

545 on the manuscript.

546

547 **Competing interests**

548 The authors declare no competing financial interests.

549

559   thank J. White (Baylor University) for useful comments on the manuscript.

560

561   **References**

562   Balseiro, D., and Powell, M. G.: Carbonate collapse and the late Paleozoic ice age marine biodiversity crisis, Geology, 48,

563   https://doi.org/10.1130/G46858.1, 2019.

564   Beerling, D. J., and Berner, R. A.: Impact of a Permo-Carboniferous high O_2 event on the terrestrial carbon cycle, Proc. Natl.

565   Acad. Sci. U.S.A., 97, 12428–12432, https://doi.org/10.1073/pnas.220280097, 2000.

566   Beerling, D. J., Woodward, F. I., Lomas, M. R., Wills, M. A., Quick, W. P., and Valdes, P. J.: The influence of

567   Carboniferous palaeoatmospheres on plant function: an experimental and modelling assessment, Philos. T. Roy. Soc. Lond.

568   B, 353, 131–140, https://doi.org/10.1098/rstb.1998.0196, 1998.

569   Belt, E. S., Heckel, P. H., Lentz, L. J., Bragonier, W. A., and Lyons, T. W.: Record of glacial–eustatic sea-level fluctuations

570   in complex middle to late Pennsylvanian facies in the Northern Appalachian Basin and relation to similar events in the

571   Midcontinent basin, Sediment. Geol., 238, 79–100, https://doi.org/10.1016/j.sedgeo.2011.04.004, 2011.

572   Benton, M. J.: No gap in the Middle Permian record of terrestrial vertebrates, Geology, 40, 339-342,

573   https://doi.org/10.1130/G32669.1, 2012.

574   Berner, R. A., and Caldeira, K.: The need for mass balance and feedback in the geochemical carbon cycle, Geology, 25,

575   955–956, https://doi.org/10.1130/0091-7613(1997)025<0955:TNFMBA>2.3.CO;2, 1997.

576   Breecker, D. O.: Quantifying and understanding the uncertainty of atmospheric CO_2 concentrations determined from calcic

577   paleosols, Geochem. Geophys. Geosy., 14, 3210–3220, https://doi.org/10.1002/ggge.20189, 2013.

578   Buggisch, W., Wang, X., Alekseev, A. S., and Joachimski, M. M.: Carboniferous–Permian carbon isotope stratigraphy of

579   successions from China (Yangtze platform), USA (Kansas) and Russia (Moscow Basin and Urals), Palaeogeogr. Palaeocl.,

580   301, 18–38, https://doi.org/10.1016/j.palaeo.2010.12.015, 2011.

581   Cagliari, J., Philipp, R. P., Buso, V. V., Netto, R. G., Klaus Hillebrand, P., da Cunha Lopes, R., Stipp Basei, M. A., and

582   Faccini, U. F.: Age constraints of the glaciation in the Paraná Basin: evidence from new U–Pb dates, J. Geol. Soc. London,

583   173, 871–874, https://doi.org/10.1144/jgs2015-161, 2016.

Cascales-Miñana, B., Diez, J. B., Gerrienne, P., and Cleal, C. J.: A palaeobotanical perspective on the great end-Permian biotic crisis, Hist. Biol., 28, 1066–1074, https://doi.org/10.1080/08912963.2015.1103237, 2016.

Caves, J. K., Jost, A. B., Lau, K. V., and Maher, K.: Cenozoic carbon cycle imbalances and a variable weathering feedback, Earth Planet. Sci. Lett., 450, 152–163, https://doi.org/10.1016/j.epsl.2016.06.035, 2016.

Chen, J., Montañez, I. P., Qi, Y., Shen, S., and Wang, X.: Strontium and carbon isotopic evidence for decoupling of $p\mathrm{CO_2}$ from continental weathering at the apex of the late Paleozoic glaciation, Geology, 46, 395–398, https://doi.org/10.1130/G40093.1, 2018.

Chen, J., and Xu, Y.-g.: Establishing the link between Permian volcanism and biodiversity changes: Insights from geochemical proxies, Gondwana Res., 75, 68–96, https://doi.org/10.1016/j.gr.2019.04.008, 2019.

Chen, J., Chen, B., and Montañez, I. P.: Carboniferous isotope stratigraphy, in: The Carboniferous Timescale, edited by: Lucas, S. G., Schneider, J. W., Wang, X., and Nikolaeva, S., Geological Society of London, London, in press.

Clapham, M. E., and James, N. P.: Paleoecology Of Early–Middle Permian Marine Communities In Eastern Australia: Response To Global Climate Change In the Aftermath Of the Late Paleozoic Ice Age, Palaios, 23, 738–750, https://doi.org/10.2110/palo.2008.p08-022r, 2008.

Cleal, C. J., and Thomas, B. A.: Palaeozoic tropical rainforests and their effect on global climates: is the past the key to the present?, Geobiology, 3, 13–31, https://doi.org/10.1111/j.1472-4669.2005.00043.x, 2005.

Crowley, T. J., and Baum, S. K.: Modeling late Paleozoic glaciation, Geology, 20, 507–510, https://doi.org/10.1130/0091-7613(1992)020<0507:MLPG>2.3.CO;2, 1992.

D'Antonio, M. P., Ibarra, D. E., and Boyce, C. K.: Land plant evolution decreased, rather than increased, weathering rates, Geology, 48, 29–33, https://doi.org/10.1130/G46776.1, 2019.

Davydov, V. I.: Precaspian Isthmus emergence triggered the Early Sakmarian glaciation: Evidence from the Lower Permian of the Urals, Russia, Palaeogeogr. Palaeocl., 511, 403–418, https://doi.org/10.1016/j.palaeo.2018.09.007, 2018.

de Boer, H. J., Drake, P. L., Wendt, E., Price, C. A., Schulze, E.-D., Turner, N. C., Nicolle, D., and Veneklaas, E. J.: Apparent Overinvestment in Leaf Venation Relaxes Leaf Morphological Constraints on Photosynthesis in Arid Habitats, Plant Physiol., 172, 2286–2299, https://doi.org/10.1104/pp.16.01313, 2016.

Dessert, C., Dupré, B., François, L. M., Schott, J., Gaillardet, J., Chakrapani, G., and Bajpai, S.: Erosion of Deccan Traps

determined by river geochemistry: impact on the global climate and the 87Sr/86Sr ratio of seawater, Earth Planet. Sci. Lett.,

188, 459–474, https://doi.org/10.1016/S0012-821X(01)00317-X, 2001.

Dessert, C., Dupré, B., Gaillardet, J., François, L. M., and Allègre, C. J.: Basalt weathering laws and the impact of basalt

weathering on the global carbon cycle, Chem. Geol., 202, 257–273, https://doi.org/10.1016/j.chemgeo.2002.10.001, 2003.

Diefendorf, A. F., Leslie, A. B., and Wing, S. L.: Leaf wax composition and carbon isotopes vary among major conifer

groups, Geochim. Cosmochim. Acta, 170, 145–156, https://doi.org/10.1016/j.gca.2015.08.018, 2015.

DiMichele, W. A., Montañez, I. P., Poulsen, C. J., and Tabor, N. J.: Climate and vegetational regime shifts in the late

Paleozoic ice age earth, Geobiology, 7, 200–226, https://doi.org/10.1111/j.1472-4669.2009.00192.x, 2009.

DiMichele, W. A., Wagner, R. H., Bashforth, A. R., and Álvárez-Vazquez, C.: An update on the flora of the Kinney Quarry

of central New Mexico (Upper Pennsylvanian), its preservational and environmental significance, in: Carboniferous-Permian

transition in central New Mexico, edited by: Lucas, S. G., Nelson, W. J., DiMichele, W. A., Speilmann, J. A., Krainer, K.,

Barrick, J. E., Elrick, S., and Voigt, S., New Mexico Museum of Natural History and Science, Bulletin, New Mexico

Museum of Natural History and Science, Albuquerque, New Mexico, 289–325, 2013.

Donnadieu, Y., Goddéris, Y., Ramstein, G., Nédélec, A., and Meert, J.: A 'snowball Earth' climate triggered by continental

break-up through changes in runoff, Nature, 428, 303–306, https://doi.org/10.1038/nature02408, 2004.

Donnadieu, Y., Goddéris, Y., Pierrehumbert, R., Dromart, G., Fluteau, F., and Jacob, R.: A GEOCLIM simulation of

climatic and biogeochemical consequences of Pangea breakup, Geochem. Geophys. Geosy., 7,

https://doi.org/10.1029/2006GC001278, 2006.

Eros, J. M., Montañez, I. P., Osleger, D. A., Davydov, V. I., Nemyrovska, T. I., Poletaev, V. I., and Zhykalyak, M. V.:

Sequence stratigraphy and onlap history of the Donets Basin, Ukraine: insight into Carboniferous icehouse dynamics,

Palaeogeogr. Palaeocl., 313, 1–25, https://doi.org/10.1016/j.palaeo.2011.08.019, 2012.

Falcon-Lang, H. J., Nelson, W. J., Heckel, P. H., DiMichele, W. A., and Elrick, S. D.: New insights on the stepwise collapse

of the Carboniferous Coal Forests: Evidence from cyclothems and coniferopsid tree-stumps near the Desmoinesian–

Missourian boundary in Peoria County, Illinois, USA, Palaeogeogr. Palaeocl., 490, 375–392,

https://doi.org/10.1016/j.palaeo.2017.11.015, 2018.

Feulner, G.: Formation of most of our coal brought Earth close to global glaciation, Proc. Natl. Acad. Sci. U.S.A., 114, 11333–11337, https://doi.org/10.1073/pnas.1712062114, 2017.

Fielding, C. R., Frank, T. D., Birgenheier, L. P., Rygel, M. C., Jones, A. T., and Roberts, J.: Stratigraphic imprint of the Late Palaeozoic Ice Age in eastern Australia: a record of alternating glacial and nonglacial climate regime, J. Geol. Soc. London, 165, 129–140, https://doi.org/10.1144/0016-76492007-036, 2008.

Fielding, C. R., Nelson, W. J., and Elrick, S. D.: Sequence stratigraphy of the late Desmoinesian to early Missourian (Pennsylvanian) succession of southern Illinois: Insights into controls on stratal architecture in an icehouse period of Earth history, J. Sediment. Res., 90, 200-227, https://doi.org/10.2110/jsr.2020.10, 2020.

Foster, G. L., Royer, D. L., and Lunt, D. J.: Future climate forcing potentially without precedent in the last 420 million years, Nat. Commun., 8, 14845, https://doi.org/10.1038/ncomms14845, 2017.

Franks, P. J., Royer, D. L., Beerling, D. J., Van de Water, P. K., Cantrill, D. J., Barbour, M. M., and Berry, J. A.: New constraints on atmospheric CO_2 concentration for the Phanerozoic, Geophys. Res. Lett., 41, 4685–4694, https://doi.org/10.1002/2014GL060457, 2014.

Friedman, M., and Sallan, L. C.: Five hundred million years of extinction and recovery: a phanerozoic survey of large-scale diversity patterns in fishes, Palaeontology, 55, 707–742, https://doi.org/10.1111/j.1475-4983.2012.01165.x, 2012.

Gaillardet, J., Dupré, B., Louvat, P., and Allègre, C. J.: Global silicate weathering and CO_2 consumption rates deduced from the chemistry of large rivers, Chem. Geol., 159, 3–30, https://doi.org/10.1016/S0009-2541(99)00031-5, 1999.

Gao, Z., Tian, W., Wang, L., Shi, L., and Pan, M.: Emplacement of intrusions of the Tarim Flood Basalt Province and their impacts on oil and gas reservoirs: A 3D seismic reflection study in Yingmaili fields, Tarim Basin, northwest China, Interpretation, 5, SK51–SK63, https://doi.org/10.1190/INT-2016-0165.1, 2017.

Gerhart, L. M., and Ward, J. K.: Plant responses to low [CO_2] of the past, New Phytol., 188, 674–695, https://doi.org/10.1111/j.1469-8137.2010.03441.x, 2010.

Gibbs, M. T., Bluth, G. J., Fawcett, P. J., and Kump, L. R.: Global chemical erosion over the last 250 my; variations due to changes in paleogeography, paleoclimate, and paleogeology, Am. J. Sci., 299, 611-651, https://doi.org/10.2475/ajs.299.7-

659   9.611, 1999.

660   Glasspool, I., Scott, A., Waltham, D., Pronina, N., and Shao, L.: The impact of fire on the Late Paleozoic Earth system,

661   Front. Plant Sci., 6, https://doi.org/10.3389/fpls.2015.00756, 2015.

662   Goddéris, Y., Donnadieu, Y., Le Hir, G., Lefebvre, V., and Nardin, E.: The role of palaeogeography in the Phanerozoic

663   history of atmospheric CO_2 and climate, Earth-Sci. Rev., 128, 122–138, https://doi.org/10.1016/j.earscirev.2013.11.004,

664   2014.

665   Goddéris, Y., Donnadieu, Y., Carretier, S., Aretz, M., Dera, G., Macouin, M., and Regard, V.: Onset and ending of the late

666   Palaeozoic ice age triggered by tectonically paced rock weathering, Nat. Geosci., 10, 382–386,

667   https://doi.org/10.1038/ngeo2931, 2017.

668   Griffis, N. P., Mundil, R., Montañez, I. P., Isbell, J., Fedorchuk, N., Vesely, F., Iannuzzi, R., and Yin, Q.-Z.: A new

669   stratigraphic framework built on U-Pb single-zircon TIMS ages and implications for the timing of the penultimate icehouse

670   (Paraná Basin, Brazil), Geol. Soc. Am. Bull., 130, 848–858, https://doi.org/10.1130/B31775.1, 2018.

671   Griffis, N. P., Montañez, I. P., Mundil, R., Richey, J. D., Isbell, J., Fedorchuk, N., Linol, B., Iannuzzi, R., Vesely, F., Mottin,

672   T., de Rosa, E., Keller, C. B., and Yin, Q.-Z.: Coupled stratigraphic and U-Pb zircon age constraints on the late Paleozoic

673   icehouse-to-greenhouse turnover in south-central Gondwana, Geology, 47, 1146–1150, https://doi.org/10.1130/G46740.1,

674   2019.

675   Grossman, E. L., Yancey, T. E., Jones, T. E., Bruckschen, P., Chuvashov, B., Mazzullo, S. J., and Mii, H.-s.: Glaciation,

676   aridification, and carbon sequestration in the Permo-Carboniferous: The isotopic record from low latitudes, Palaeogeogr.

677   Palaeocl., 268, 222–233, https://doi.org/10.1016/j.palaeo.2008.03.053, 2008.

678   Groves, J. R., and Yue, W.: Foraminiferal diversification during the late Paleozoic ice age, Paleobiology, 35, 367–392,

679   https://doi.org/10.1666/0094-8373-35.3.367, 2009.

680   Henderson, C. M., Wardlaw, B. R., Davydov, V. I., Schmitz, M. D., Schiappa, T. A., Tierney, K. E., and Shen, S.: Proposal

681   for base-Kungurian GSSP, Permophiles, 56, 8–21, 2012.

682   Hernandez-Castillo, G. R., Stockey, R. A., Mapes, G. K., and Rothwell, G. W.: A new voltzialean conifer *Emporia royalii*

683   sp. nov. (Emporiaceae) from the Hamilton Quarry, Kansas, Int. J. Plant Sci., 170, 1201–1227,

684   https://doi.org/10.1086/605874, 2009a.

685   Hernandez-Castillo, G. R., Stockey, R. A., Rothwell, G. W., and Mapes, G. K.: Reconstruction of the Pennsylvanian-age

686   walchian conifer *Emporia cryptica* sp. nov. (Emporiaceae: Voltziales), Rev. Palaeobot. Palyno., 157, 218–237,

687   https://doi.org/10.1016/j.revpalbo.2009.05.003, 2009b.

688   Hernandez-Castillo, G. R., Stockey, R. A., Rothwell, G. W., and Mapes, G. K.: Reconstructing *Emporia lockardii*

689   (Voltziales: Emporiaceae) and initial thoughts on Paleozoic conifer ecology, Int. J. Plant Sci., 170, 1056–1074,

690   https://doi.org/10.1086/605115, 2009c.

691   Hibbett, D., Blanchette, R., Kenrick, P., and Mills, B.: Climate, decay, and the death of the coal forests, Curr. Biol., 26,

692   R563–R567, https://doi.org/10.1016/j.cub.2016.01.014, 2016.

693   Horton, D. E., Poulsen, C. J., Montañez, I. P., and DiMichele, W. A.: Eccentricity-paced late Paleozoic climate change,

694   Palaeogeogr. Palaeocl., 331, 150–161, https://doi.org/10.1016/j.palaeo.2012.03.014, 2012.

695   Ibarra, D. E., Caves, J. K., Moon, S., Thomas, D. L., Hartmann, J., Chamberlain, C. P., and Maher, K.: Differential

696   weathering of basaltic and granitic catchments from concentration–discharge relationships, Geochim. Cosmochim. Acta,

697   190, 265–293, https://doi.org/10.1016/j.gca.2016.07.006, 2016.

698   Ibarra, D. E., Rugenstein, J. K. C., Bachan, A., Baresch, A., Lau, K. V., Thomas, D. L., Lee, J.-E., Boyce, C. K., and

699   Chamberlain, C. P.: Modeling the consequences of land plant evolution on silicate weathering, Am. J. Sci., 319, 1–43,

700   https://doi.org/10.2475/01.2019.01, 2019.

701   Isbell, J. L., Henry, L. C., Gulbranson, E. L., Limarino, C. O., Fraiser, M. L., Koch, Z. J., Ciccioli, P. L., and Dineen, A. A.:

702   Glacial paradoxes during the late Paleozoic ice age: Evaluating the equilibrium line altitude as a control on glaciation,

703   Gondwana Res., 22, 1–19, https://doi.org/10.1016/j.gr.2011.11.005, 2012.

704   Joshi, M. M., Mills, B. J. W., and Johnson, M.: A Capacitor-Discharge Mechanism to Explain the Timing of Orogeny-

705   Related Global Glaciations, Geophys. Res. Lett., 46, 8347-8354, https://doi.org/10.1029/2019GL083368, 2019.

706   Käßner, A., Tichomirowa, M., Lützner, H., and Gaupp, R.: New high precision CA-ID-TIMS U-Pb zircon ages from the

707   Thuringian Forest Rotliegend section, in: Geophysical Research Abstracts, European Geophysical Union, Vienna, Austria,

708   2019,

Kemp, T. S.: The origin and early radiation of the therapsid mammal-like reptiles: a palaeobiological hypothesis, J. Evolution. Biol., 19, 1231–1247, https://doi.org/10.1111/j.1420-9101.2005.01076.x, 2006.

Koch, J. T., and Frank, T. D.: The Pennsylvanian–Permian transition in the low-latitude carbonate record and the onset of major Gondwanan glaciation, Palaeogeogr. Palaeocl., 308, 362–372, https://doi.org/10.1016/j.palaeo.2011.05.041, 2011.

Korte, C., and Ullmann, C. V.: Permian strontium isotope stratigraphy, Geol. Soc. Spec. Publ., 450, 105–118, https://doi.org/10.1144/sp450.5, 2018.

Krause, A. J., Mills, B. J. W., Zhang, S., Planavsky, N. J., Lenton, T. M., and Poulton, S. W.: Stepwise oxygenation of the Paleozoic atmosphere, Nat. Commun., 9, https://doi.org/10.1038/s41467-018-06383-y, 2018.

Lee, C.-T. A., Thurner, S., Paterson, S., and Cao, W.: The rise and fall of continental arcs: Interplays between magmatism, uplift, weathering, and climate, Earth Planet. Sci. Lett., 425, 105–119, https://doi.org/10.1016/j.epsl.2015.05.045, 2015.

Lee, C.-T. A., and Dee, S.: Does volcanism cause warming or cooling?, Geology, 47, 687–688, https://doi.org/10.1130/focus072019.1, 2019.

Lenton, T. M., Daines, S. J., and Mills, B. J. W.: COPSE reloaded: An improved model of biogeochemical cycling over Phanerozoic time, Earth-Sci. Rev., 178, 1–28, https://doi.org/10.1016/j.earscirev.2017.12.004, 2018.

Li, H., Taylor, E. L., and Taylor, T. N.: Permian Vessel Elements, Science, 271, 188–189, https://doi.org/10.1126/science.271.5246.188, 1996.

Lowry, D. P., Poulsen, C. J., Horton, D. E., Torsvik, T. H., and Pollard, D.: Thresholds for Paleozoic ice sheet initiation, Geology, 42, 627–630, https://doi.org/10.1130/G35615.1, 2014.

Macdonald, F. A., Swanson-Hysell, N. L., Park, Y., Lisiecki, L., and Jagoutz, O.: Arc-continent collisions in the tropics set Earth's climate state, Science, 364, 181–184, https://doi.org/10.1126/science.aav5300, 2019.

Maher, K., and Chamberlain, C. P.: Hydrologic Regulation of Chemical Weathering and the Geologic Carbon Cycle, Science, 343, 1502–1504, https://doi.org/10.1126/science.1250770, 2014.

McGhee, G. R.: Carboniferous Giants and Mass Extinction: The Late Paleozoic Ice Age World, Columbia University Press, New York, 2018.

McKenzie, N. R., Horton, B. K., Loomis, S. E., Stockli, D. F., Planavsky, N. J., and Lee, C.-T. A.: Continental arc volcanism

734   as the principal driver of icehouse-greenhouse variability, Science, 352, 444–447, https://doi.org/10.1126/science.aad5787,

735   2016.

736   McLoughlin, S.: Glossopteris–insights into the architecture and relationships of an iconic Permian Gondwanan plant, J. Bot.

737   Soc. Bengal, 65, 93–106, 2011.

738   Melville, R.: Glossopteridae, Angiospermidae and the evidence for angiosperm origin, Bot. J. Linn. Soc., 86, 279–323,

739   https://doi.org/10.1111/j.1095-8339.1983.tb00975.x, 1983.

740   Montañez, I. P.: Modern soil system constraints on reconstructing deep-time atmospheric CO_2, Geochim. Cosmochim. Acta,

741   101, 57–75, https://doi.org/10.1016/j.gca.2012.10.012, 2013.

742   Montañez, I. P.: A Late Paleozoic climate window of opportunity, Proc. Natl. Acad. Sci. U.S.A., 113, 2234–2336,

743   https://doi.org/10.1073/pnas.1600236113, 2016.

744   Montañez, I. P., and Poulsen, C. J.: The Late Paleozoic Ice Age: An Evolving Paradigm, Annu. Rev. Earth Pl. Sc., 41, 629–

745   656, https://doi.org/10.1146/annurev.earth.031208.100118, 2013.

746   Montañez, I. P., Tabor, N. J., Niemeier, D., DiMichele, W. A., Frank, T. D., Fielding, C. R., Isbell, J. L., Birgenheier, L. P.,

747   and Rygel, M. C.: CO_2-forced climate and vegetation instability during Late Paleozoic deglaciation, Science, 315, 87–91,

748   https://doi.org/10.1126/science.1134207, 2007.

749   Montañez, I. P., McElwain, J. C., Poulsen, C. J., White, J. D., Dimichele, W. A., Wilson, J. P., Griggs, G., and Hren, M. T.:

750   Climate, $p$$CO_2$ and terrestrial carbon cycle linkages during late Palaeozoic glacial–interglacial cycles, Nat. Geosci., 9, 824–

751   828, https://doi.org/10.1038/ngeo2822, 2016.

752   Ogg, J. G., Ogg, G., and Gradstein, F. M.: A concise geologic time scale: 2016, Elsevier, New York, 2016.

753   Pardo, J. D., Small, B. J., Milner, A. R., and Huttenlocker, A. K.: Carboniferous–Permian climate change constrained early

754   land vertebrate radiations, Nat. Ecol. Evol., 3, 200–206, https://doi.org/10.1038/s41559-018-0776-z, 2019.

755   Poulsen, C. J., Tabor, C., and White, J. D.: Long-term climate forcing by atmospheric oxygen concentrations, Science, 348,

756   1238–1241, https://doi.org/10.1126/science.1260670, 2015.

757   Richey, J. D., Montañez, I. P., Goddéris, Y., Looy, C. V., Griffis, N. P., and DiMichele, W. A.: Primary Data from Richey et

758   al., 2020 (Climate Of The Past), https://doi.org/10.25338/B8S90Q, 2020.

759   Romanek, C. S., Grossman, E. L., and Morse, J. W.: Carbon isotopic fractionation in synthetic aragonite and calcite: Effects

760   of temperature and precipitation rate, Geochim. Cosmochim. Acta, 56, 419–430, https://doi.org/10.1016/0016-

761   7037(92)90142-6, 1992.

762   Sato, A. M., Llambías, E. J., Basei, M. A. S., and Castro, C. E.: Three stages in the Late Paleozoic to Triassic magmatism of

763   southwestern Gondwana, and the relationships with the volcanogenic events in coeval basins, J. S. Am. Earth Sci., 63, 48–

764   69, https://doi.org/10.1016/j.jsames.2015.07.005, 2015.

765   Scotese, C.: PALEOMAP PaleoAtlas for GPlates and the PaleoData Plotter Program, PALEOMAP Project,

766   https://www.earthbyte.org/paleomap-paleoatlas-for-gplates/, 2016.

767   Shellnutt, J. G.: The Panjal Traps, in: Large Igneous Provinces from Gondwana and Adjacent Regions, edited by: Sensarma,

768   S., and Storey, B. C., Special Publications, 1, Geological Society, London, 59–86, 2018.

769   Šimůnek, Z.: Cuticular analysis of new Westphalian and Stephanian Cordaites species from the USA, Rev. Palaeobot.

770   Palyno., 253, 1–14, https://doi.org/10.1016/j.revpalbo.2018.03.001, 2018.

771   Soreghan, G. S., Soreghan, M. J., and Heavens, N. G.: Explosive volcanism as a key driver of the late Paleozoic ice age,

772   Geology, 47, 600–604, https://doi.org/10.1130/G46349.1, 2019.

773   Spalletti, L. A., and Limarino, C. O.: The Choiyoi magmatism in south western Gondwana: implications for the end-permian

774   mass extinction-a review, Andean Geol., 44, 328–338, http://dx.doi.org/10.5027/andgeoV44n3-a05, 2017.

775   Srivastava, A. K.: Evolutionary tendency in the venation pattern of Glossopteridales, Geobios, 24, 383–386,

776   https://doi.org/10.1016/S0016-6995(06)80235-4, 1991.

777   Stanley, S. M.: Estimates of the magnitudes of major marine mass extinctions in earth history, Proc. Natl. Acad. Sci. U.S.A.,

778   113, E6325–E6334, https://doi.org/10.1073/pnas.1613094113, 2016.

779   Stanley, S. M., and Powell, M. G.: Depressed rates of origination and extinction during the late Paleozoic ice age: a new

780   state for the global marine ecosystem, Geology, 31, 877–880, https://doi.org/10.1130/G19654R.1, 2003.

781   Tabor, N. J., and Montañez, I. P.: Oxygen and hydrogen isotope compositions of Permian pedogenic phyllosilicates:

782   development of modern surface domain arrays and implications for paleotemperature reconstructions, Palaeogeogr.

783   Palaeocl., 223, 127–146, https://doi.org/10.1016/j.palaeo.2005.04.009, 2005.

784 Tabor, N. J., DiMichele, W. A., Montañez, I. P., and Chaney, D. S.: Late Paleozoic continental warming of a cold tropical
785 basin and floristic change in western Pangea, Int. J. Coal. Geol., 119, 177–186, https://doi.org/10.1016/j.coal.2013.07.009,
786 2013.

787 Torsvik, T. H., Smethurst, M. A., Burke, K., and Steinberger, B.: Long term stability in deep mantle structure: Evidence
788 from the ~300 Ma Skagerrak-Centered Large Igneous Province (the SCLIP), Earth Planet. Sci. Lett., 267, 444–452,
789 https://doi.org/10.1016/j.epsl.2007.12.004, 2008.

790 Walker, J. C. G., Hays, P. B., and Kasting, J. F.: A negative feedback mechanism for the long-term stabilization of Earth's
791 surface temperature, J. Geophys. Res.-Oceans, 86, 9776–9782, https://doi.org/10.1029/JC086iC10p09776, 1981.

792 Wang, X.-D., Wang, X.-J., Zhang, F., and Zhang, H.: Diversity patterns of Carboniferous and Permian rugose corals in
793 South China, Geol. J., 41, 329–343, https://doi.org/10.1002/gj.1041, 2006.

794 West, A. J.: Thickness of the chemical weathering zone and implications for erosional and climatic drivers of weathering and
795 for carbon-cycle feedbacks, Geology, 40, 811–814, https://doi.org/10.1130/g33041.1, 2012.

796 Wilson, J. P., Montañez, I. P., White, J. D., DiMichele, W. A., McElwain, J. C., Poulsen, C. J., and Hren, M. T.: Dynamic
797 Carboniferous tropical forests: new views of plant function and potential for physiological forcing of climate, New Phytol.,
798 215, 1333–1353, https://doi.org/10.1111/nph.14700, 2017.

799 Wilson, J. P., White, J. D., Montañez, I. P., DiMichele, W. A., McElwain, J. C., Poulsen, C. J., and Hren, M. T.:
800 Carboniferous plant physiology breaks the mold, New Phytol., https://doi.org/10.1111/nph.16460, 2020.

801 Yang, S., Chen, H., Li, Z., Li, Y., Yu, X., Li, D., and Meng, L.: Early Permian Tarim Large Igneous Province in northwest
802 China, Sci. China Earth Sci., 56, 2015–2026, https://doi.org/10.1007/s11430-013-4653-y, 2013.

803 Zhai, Q.-g., Jahn, B.-m., Su, L., Ernst, R. E., Wang, K.-l., Zhang, R.-y., Wang, J., and Tang, S.: SHRIMP zircon U–Pb
804 geochronology, geochemistry and Sr–Nd–Hf isotopic compositions of a mafic dyke swarm in the Qiangtang terrane,
805 northern Tibet and geodynamic implications, Lithos, 174, 28–43, https://doi.org/10.1016/j.lithos.2012.10.018, 2013.

806 Zhou, W., Wan, M., Koll, R. A., and Wang, J.: Occurrence of the earliest gigantopterid from the basal Permian of the North
807 China Block and its bearing on evolution, Geol. J., 53, 500–509, https://doi.org/10.1002/gj.2907, 2017.